

Hierarchical Physics-Embedded Learning for Prediction and Discovery in Spatiotemporal Dynamical Systems

Xizhe Wang^{1*}, Xiaobin Song^{1*}, Qingshan Jia¹, Hao Sun^{2†}, Hongbo Zhao^{3†}, and Benben Jiang^{1†}

1 CFINS, Department of Automation, Beijing National Research Center for Information Science and Technology, Tsinghua University, Beijing 100084, China

2 Gaoling School of Artificial Intelligence, Renmin University of China, Beijing 100086, China

3 Department of Physics, Department of Chemistry and Biochemistry, University of California, San Diego, CA 92093, USA

** These authors contributed equally to this work*

† Corresponding authors

Abstract

Modeling complex spatiotemporal dynamics, particularly in far-from-equilibrium systems, remains a grand challenge in science. The governing partial differential equations (PDEs) for these systems are often intractable to derive from first principles, due to their inherent complexity—characterized by high-order derivatives and strong nonlinearities—coupled with incomplete physical knowledge. This has spurred the development of data-driven methods, yet these approaches face limitations: Purely data-driven models are often physically inconsistent and data-intensive, while existing physics-informed methods lack the structural capacity to represent complex operators or systematically integrate partial physical knowledge. Here, we propose a hierarchical physics-embedded learning framework that fundamentally advances both the forward spatiotemporal prediction and inverse discovery of physical laws from sparse and noisy data. The key innovation is a two-level architecture that mirrors the process of scientific discovery: the first level learns fundamental symbolic components of a PDE, while the second learns their governing combinations. This hierarchical decomposition not only reduces learning complexity but, more importantly, enables a structural integration of prior knowledge. Known physical laws are directly embedded into the model’s computational graph, guaranteeing physical consistency and improving data efficiency. By building the framework upon adaptive Fourier Neural Operators, we can effectively capture the non-local dependencies and high-order operators characteristic of dynamical systems. Additionally, by structurally decoupling known and unknown terms, the framework further enables interpretable discovery of underlying governing equations through symbolic regression, without presupposing functional forms. Theoretically, we

derive an explicit error decomposition for the proposed hierarchical framework, and the universal approximation property of Fourier attention for high-order differential operators. We validate the approach on various spatiotemporal dynamical systems, demonstrating superior performance than baseline methods. These results establish a powerful, generalizable methodology for spatiotemporal dynamics modeling and governing equations discovery in complex dynamical systems.

1 Introduction

Partial differential equations (PDEs) serve as foundational tools for modeling the spatiotemporal dynamics of natural and engineered systems^{1,2}. They provide compact and interpretable descriptions of physical processes such as transport³, reaction^{4,5}, and pattern formation^{6,7}, and are extensively used across disciplines^{8–10}. A limited number of governing equations such as the diffusion or wave equation can be derived from first principles and solved using well-established analytical or numerical techniques^{11,12}. Yet, many real-world systems exhibit multiscale and structural complexity that renders such first-principle derivations intractable. Modeling long spatiotemporal scales often requires closure relations that link fine-grained variables to coarse observables, which are difficult to establish even when microscopic equations of motion are known, especially in strongly interacting systems^{13–17}. In such cases, constitutive relations—such as nonlinear reaction kinetics, stress–strain laws, or transport coefficients—are often phenomenological, history-dependent, nonlocal, or involving high-order derivatives, limiting their predictive power. Turbulence^{14,15} exemplifies this challenge: despite centuries of study, its quantitative modeling remains elusive, though it is central to earth and climate sciences. Similarly, in health and materials science, the absence of general models for far-from-equilibrium systems makes prediction in living organisms and energy materials particularly difficult^{16,17}.

To capture the essence of such spatiotemporal dynamical systems, canonical nonequilibrium models have been developed to describe emergent pattern formation^{18,19}. The Cahn–Hilliard (CH) equation^{20,21}, for instance, characterizes phase separation through nucleation, growth, and spinodal decomposition, governed by conserved order-parameter dynamics descending along a free-energy landscape under constraints of mass conservation and thermodynamics. The complex Ginzburg–Landau (CGL) equation²², derived from weakly nonlinear expansions near instability onset, captures universal oscillatory behaviors with minimal polynomial terms, and has been applied broadly in reaction–diffusion systems and nonlinear optics. While these models are parsimonious, interpretable, and universal, they often fall short in providing quantitative predictions for specific systems, especially when underlying dynamical laws or constitutive relations remain unknown or experimentally

inaccessible. These limitations have motivated the development of data-driven methods for modeling spatiotemporal dynamics directly from data.

Conventional approaches, such as dynamic mode decomposition (DMD)^{23–25}, rely on projecting high-dimensional data onto low-dimensional linear subspaces, offering interpretability and efficiency but limited expressiveness for nonlinear, multiscale systems. Deep learning methods^{26–30} offer a more flexible alternative, capable of learning complex mappings from sparse or noisy data to the underlying spatiotemporal dynamics. However, purely data-driven approaches face significant challenges when applied to physical problems. Although these methods are designed to fit observed data, their predictions may violate fundamental physical constraints and often require large amounts of labeled data to generalize across different regimes. Therefore, it is crucial to incorporate physical constraints or prior knowledge such as partial information about the PDE into the learning process. This not only enhances the physical consistency of data-driven predictions, but also reduces the complexity of learning unknown physical PDEs de novo.

One possible solution is to incorporate governing equations directly into the training process, as exemplified by physics-informed neural networks (PINNs)^{31–36}. PINNs impose soft constraints on the solution by minimizing the residuals of PDEs, along with associated initial and boundary conditions, through a regularized loss formulation. While effective in many forward and inverse problems, PINNs face optimization challenges due to the competition between multiple loss terms and lack the ability to hard-encode prior physics into the model. To overcome these limitations, physics-encoded neural networks (PENNs)^{37,38} have been proposed to incorporate known physics structure directly into the network architecture. A representative example is the physics-encoded recurrent convolutional neural network (PeRCNN)³⁸, which uses convolutional layers to approximate spatial derivatives and recurrent modules to capture temporal dynamics. By structurally encoding known physical operators into the network design, PeRCNN improves physical consistency and data efficiency. However, its reliance on local convolutions imposes fundamental limits on receptive field size, which restricts its ability to accurately approximate high-order derivatives or capture long-range spatial interactions. More fundamentally, PeRCNN represents PDEs as linear combinations of differential terms approximated by local convolutional operations, which inherently constrains the model to polynomial-like expressions. Although this design is effective for systems governed by standard equations such as diffusion and reaction processes, it is insufficient for capturing the structural complexity of nonequilibrium dynamical systems. The governing equations of such systems often involve high-order derivatives and highly nonlinear terms (such as logarithmic functions).

Recent advances in operator learning^{39–43} have provided a promising solution by directly learning mappings between function spaces. Unlike convolution-based architectures constrained by local

receptive fields, operator learning frameworks such as the Fourier Neural Operator (FNO)⁴⁰ and the Adaptive Fourier Neural Operator (AFNO)⁴¹ leverage their global structure and spectral representations to effectively model long-range spatial dependencies and approximate high-order differential operators and highly nonlinear terms that are often challenging to capture using local convolutional kernels. As a result, these models have demonstrated strong performance in learning complex physical systems governed by PDEs. Despite these architectural advantages, existing operator learning methods face two limitations. First, they typically require substantial amounts of labelled data to accurately approximate the underlying operator, which can limit their applicability in data-scarce scientific domains. Second, they offer limited mechanisms for integrating known physical constraints or partial domain knowledge into the learning process. Although recent studies^{44,45} have explored various strategies such as physics-informed architectures to address this issue, the systematic integration of prior knowledge (such as explicitly separating known and unknown components) remains an open challenge. These limitations reduce the interpretability of the learned representations and hinder the model’s ability to produce reliable predictions under temporal extrapolation, which is critical for many spatiotemporal modeling tasks.

To this end, we introduce a hierarchical physics-embedded learning framework that structurally embeds prior physical knowledge into network architectures as shown in Fig. 1, enabling accurate forward modeling and interpretable discovery of spatiotemporal dynamical systems governed by PDEs. Specifically, it incorporates three key innovations. (1) Our framework adopts a two-level hierarchical architecture that mirrors the progressive discovery process of physical laws. The first level specializes in extracting spatiotemporal features corresponding to fundamental symbolic expressions (e.g., diffusivity and free energy terms in phase-field models) with respect to state variables; and the second level learns the complex interactions and governing combinations between these fundamental expressions. This hierarchical design significantly reduces learning complexity through decomposition (particularly by lowering the order of differential operators required at each level). Moreover, we explicitly embed known physical knowledge through dedicated computational channels that bypass learning, enabling flexible integration of prior knowledge and improving both physical consistency and data efficiency. (2) Our framework employs adaptive Fourier neural operators (AFNO) to capture spatial patterns beyond the locality of convolutional kernels. By performing frequency-domain mixing through Fourier transforms and attention mechanisms, AFNO attains a global receptive field while preserving expressive flexibility. This allows the model to efficiently learn long-range dependencies and accurately represent high-order differential operators and nonlinear terms. (3) Our framework enables explicit discovery of unknown physical expressions through integration with symbolic regression. By embedding known components through dedicated computational channels and

assigning each AFNO channel to capture a distinct unknown term, the hierarchical design supports structural decoupling of complex physical interactions. The resulting intermediate representations learned by individual AFNO channels can be directly transformed into closed-form governing PDE expressions through symbolic regression, without assuming their structural form. This capability offers a principled bridge between data-driven modeling and interpretable scientific discovery. Overall, we present a hierarchical physics-embedded learning framework that offers a unified and interpretable approach for modeling complex spatiotemporal dynamics, and we validate its effectiveness on various spatiotemporal dynamical systems through forward prediction and inverse discovery tasks.

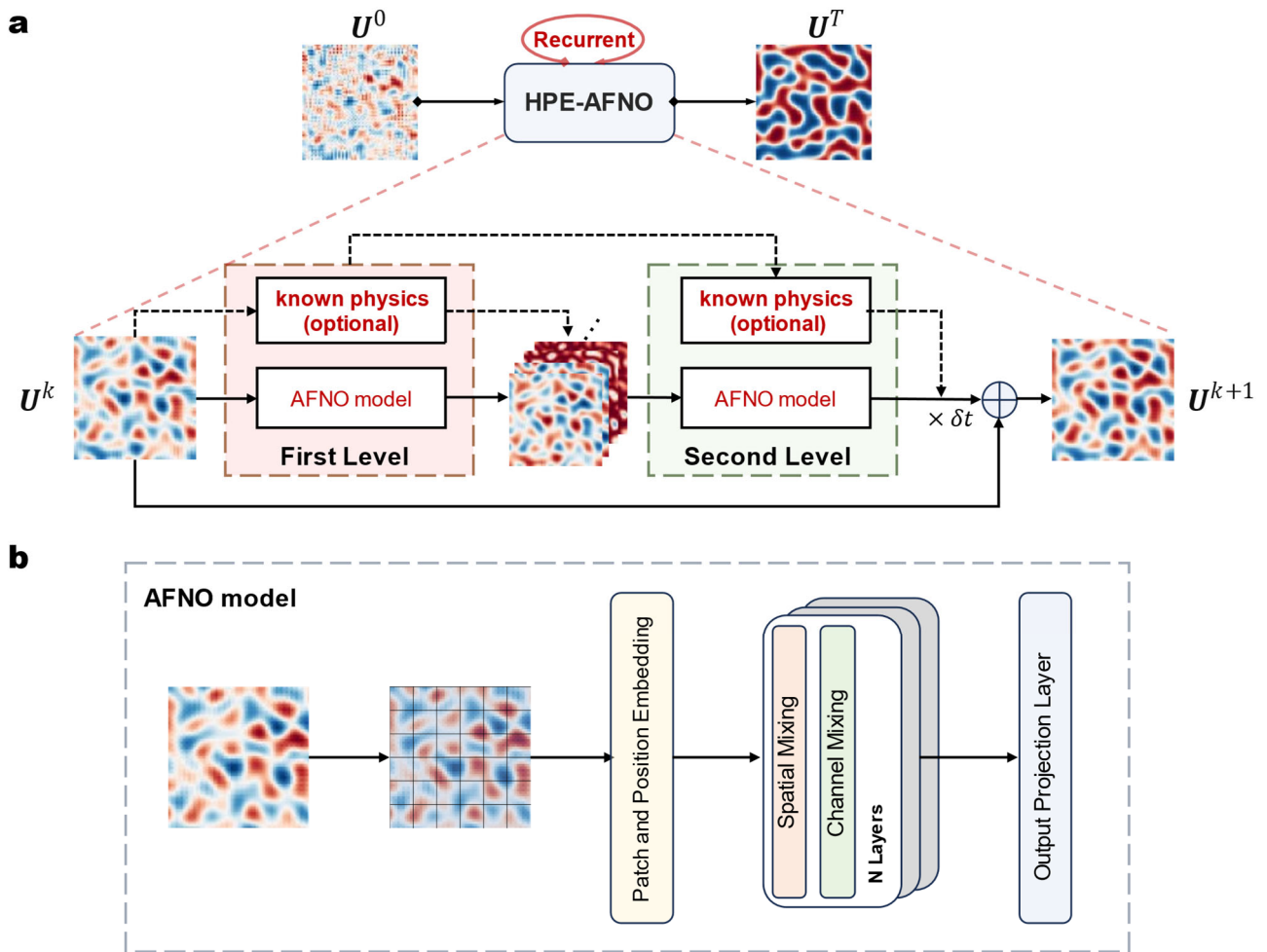


Fig. 1 | Hierarchical Physics-Embedded Adaptive Fourier Neural Operator (HPE-AFNO) framework for spatiotemporal dynamics modeling. **a**, Schematic of the two-level HPE - AFNO network, illustrating how the model can optionally incorporate known physical knowledge (e.g., diffusivity and free energy terms in phase-field models) and known governing combination rules. Two AFNO modules separately extract fundamental symbolic features from the current field U^k and learn governing combinations among them, culminating in a prediction U^{k+1} via a time - integration step δt . This hierarchical design not only reduces learning complexity through decomposition, but also enables direct and flexible embedding of known physical knowledge. **b**, Detailed architecture of the AFNO - based feature extraction pipeline. Input fields are first divided into patches with positional information, then processed through multiple spatial and channel mixing layers, ultimately projected

back to the physical domain. Fourier transforms in AFNO enhance the model’s ability to capture both local and global dynamics.

2 Results

2.1 Hierarchical physics-embedded learning for modelling spatiotemporal dynamics

(a) Learning spatiotemporal dynamics from data

PDEs are fundamental in modelling physical systems. However, a significant number of systems, particularly those in electrochemistry and biology, are governed by PDEs that remain either entirely unknown or only partially characterized. With increasing data availability and advances in scientific machine learning, data-driven modelling has emerged as an effective approach for developing predictive models of physical systems. Our proposed hierarchical physics-embedded network demonstrates exceptional capability in representing spatiotemporal dynamics and successfully incorporating incomplete governing PDEs, especially those involving high-order differential operators and strong nonlinear terms (see ‘HPE-AFNO framework’ in **Methods**). This unique capability positions it as a powerful and generalizable framework for predicting complex spatiotemporal dynamics. In this section, we focus on modeling spatiotemporal dynamics using our proposed hierarchical physics-embedded learning paradigm when only limited, noisy measurement data are available.

We assume that spatiotemporal dynamics are accessible only through a limited number of sparse and potentially noisy snapshots, denoted as $\tilde{\mathbf{U}} \in \mathbb{R}^{N_t' \times H \times W}$, collected with a sampling interval of $\delta t'$. Here, N_t' represents the total number of sparse temporal observations, and $H \times W$ indicates the spatial resolution of each state snapshot. Our objective is to construct a predictive model that provides the most likely noise-free solution $\hat{\mathbf{U}} \in \mathbb{R}^{N_t \times H \times W}$, where $N_t' < N_t$, with satisfactory interpolation capability ($t \leq t_{N_t'}$) and extrapolation performance ($t > t_{N_t'}$) across the temporal horizon.

We validate the performance of HPE-AFNO using the synthetic datasets generated by the Cahn-Hilliard (CH)^{21,46,47} equation. To evaluate the model’s ability to reconstruct spatiotemporal dynamics from sparse observations, we consider a test scenario wherein 91 snapshots are acquired from a 64×64 spatial grid at intervals of $\delta t' = 0.1$ s over the time span $t \in [0,9]$ s. The model is subsequently trained to reconstruct the system’s evolution at a refined temporal resolution of $\delta t = 0.01$ s, thereby generating 901 interpolated snapshots within the identical time window. Subsequent to the interpolation phase, we further assess the model’s extrapolation performance by predicting system states beyond the observation horizon ($t > 9$ s), maintaining the same high temporal resolution. Implementation details of HPE-AFNO are provided in **Supplementary Note 1** and **Supplementary Table 1**.

As shown in **Fig. 2a**, the HPE-AFNO model accurately reconstructs the intricate spatiotemporal dynamics of phase separation across the entire temporal domain. The predicted patterns (second row) exhibit a close resemblance to the ground truth, displaying minimal visual discrepancies throughout both the interpolation and extrapolation phases. Quantitatively, the model consistently maintains low prediction errors, as quantified by root mean square error (RMSE; detailed in **Supplementary Note 3**). Within the interpolation period ($0 \leq t \leq 9\text{s}$), HPE-AFNO achieves an average RMSE of 0.021, with a representative value of 0.015 at $t = 2.5\text{s}$. In the extrapolation regime (defined as $9\text{s} < t \leq 20\text{s}$), the error shows a moderate increase, averaging an RMSE of 0.077, with a specific value of 0.11 at $t = 18.5\text{s}$. In contrast, baseline models exhibit significantly reduced accuracy. Although PeRCNN³⁸ incorporates explicit physical priors, its predictions progressively deviate from the ground truth in later stages (fourth row, **Fig. 2a**), especially during extrapolation (e.g., RMSE = 0.27 at $t = 18.5\text{s}$). FNO-2D^{40,48} performs even less effectively under conditions of sparse observations, frequently yielding nearly time-invariant predictions (sixth row, **Fig. 2a**) and failing to capture crucial spatiotemporal variations. These qualitative trends are confirmed by the RMSE curves in Fig. 2a. Compared to PeRCNN, HPE-AFNO reduces the average RMSE by 71.2% during interpolation (0.021 vs. 0.073) and by 62.8% during extrapolation (0.077 vs. 0.207). Relative to FNO-2D, the reductions are 51.3% and 49.2%, respectively. Notably, HPE-AFNO maintains a consistent performance advantage during extrapolation, demonstrating its advantage in long-term spatiotemporal prediction tasks.

To further verify the effectiveness of the proposed HPE-AFNO method, we evaluated its performance on a diverse set of additional spatiotemporal dynamical systems, including both two- and three-dimensional cases. Specifically, we considered the two-dimensional Allen-Cahn (AC) equation^{46,49}, the deterministic Kardar-Parisi-Zhang (dKPZ) equation⁵⁰, the Complex Ginzburg-Landau (CGL) equation²², and a three-dimensional Allen-Cahn (3D-AC) system^{46,49}. These systems were selected for their broad applications in physics and materials science, distinct pattern formation mechanisms, and unique numerical challenges. Across these complex systems, results consistently show the proposed HPE-AFNO method significantly outperforming baseline approaches (**Figs. 2b-d** and **Fig. 3**). More specifically, for the dKPZ equation, characterized by nonlinear spatiotemporal dynamics, HPE-AFNO shows clear and consistent advantages, which reconstructs the system's evolution, preserving both fine-scale textures and large-scale structures over time (**Fig. 2c**). In contrast, PeRCNN's predictions exhibit a gradual loss of spatial fidelity, becoming increasingly blurred and incoherent, likely due to its intrinsic locality hindering the capture of long-range couplings typical of dKPZ evolution. FNO-2D shows a different failure mode, with outputs collapsing into quasi-static solutions that do not reflect the system's evolving nature (**Fig. 2c**). During interpolation regime ($t \leq$

9s), average RMSEs were 0.0049 for HPE-AFNO, while PeRCNN and FNO-2D were 0.018 and 0.035, respectively. In the extrapolation regime ($t > 9s$), HPE-AFNO’s average RMSE was 0.006, compared to 0.042 for PeRCNN and 0.032 for FNO-2D. This performance gap becomes increasingly pronounced in long-term prediction; for instance, at $t=18.5s$, HPE-AFNO’s error is less than half that of either baseline model. HPE-AFNO’s capacity to maintain low and stable prediction error throughout highlights its superior performance for modeling complex dKPZ dynamics.

The CGL equation poses an even more demanding test due to its strong nonlinearity, extreme sensitivity to initial conditions, and intricate spatiotemporal dynamics involving spiral waves and phase turbulence. These challenges are further intensified by the choice to represent the input using only the modulus of the complex-valued field. Without access to the real and imaginary components, the reconstruction of full spatiotemporal dynamics becomes a severely underdetermined problem, and the model is compelled to approximate phase dependent structures such as spiral cores and turbulence patterns from scalar amplitude observations alone. Under this setting, baseline model limitations are evident (**Fig. 2d**): PeRCNN initially captures local patterns but loses coherence beyond $t = 6.5s$, while FNO-2D fails to capture characteristic spiral patterns, producing distorted outputs. In contrast, HPE-AFNO shows a stronger ability to recover essential evolutionary features, including spiral core dynamics, and maintains recognizable spatiotemporal structures over longer horizons. The RMSE (**Fig. 2d**) further support these assessments. During both the interpolation ($t \leq 9s$) and extrapolation ($t > 9s$) regimes, HPE-AFNO achieves significant reductions in average RMSE compared to PeRCNN and FNO-2D.

While the previous results demonstrate the effectiveness of HPE-AFNO on various two-dimensional spatiotemporal systems, extending accurate prediction to three-dimensional cases presents a significantly more challenge. In the three-dimensional Allen–Cahn (3D-AC) system, increased degrees of freedom and stronger spatiotemporal coupling accelerate error accumulation, making the preservation of interface topology under sparse and noisy observations particularly difficult. As shown in **Fig. 3a**, HPE-AFNO reconstructs the 3D phase-field evolution with high fidelity across both interpolation and extrapolation regimes, accurately capturing progressive coarsening dynamics and maintaining coherent interface structures over the full temporal horizon. In contrast, PeRCNN suffers from a gradual degradation of interface integrity during long-term evolution, where phase boundaries become progressively blurred and eventually indiscriminable due to error accumulation. Similarly, FNO-3D fails to adequately capture the system’s underlying temporal evolution, resulting in predictions that deviate increasingly from the true dynamics during extrapolation. These qualitative differences are quantitatively reflected in the RMSE curves shown in **Fig. 3b**. HPE-AFNO maintains

consistently low error growth in the extrapolation regime, whereas both PeRCNN and FNO-3D exhibit marked error divergence beyond the interpolation phase, underscoring the efficacy of HPE-AFNO for long-term extrapolation in complex three-dimensional spatiotemporal systems.

Consistent superior performance across the CH, AC, dKPZ, CGL, and 3D-AC systems reinforces the proposed HPE-AFNO method’s clear advantages over baselines, underscoring our hierarchical physics-embedded framework’s capacity to accurately model diverse and complex spatiotemporal dynamics. This considerably superior performance stems from two key architectural innovations designed to address the core challenges of modeling complex, nonlinear PDEs. First, unlike the single-level architectures used in baseline models, our method adopts a hierarchical structure inspired by the progressive formulation of physical laws. The first level extracts fundamental symbolic expressions related to state variables, while the second level learns their governing combinations with nonlinear and higher-order interactions. This decomposition simplifies the learning process by partitioning complex PDEs into more tractable subproblems (see ‘Hierarchical error decomposition of HPE-AFNO’ in **Methods**). Second, instead of conventional local convolutions, the model employs a Fourier attention mechanism that operates in the frequency domain. This design enables efficient capture of long-range spatial dependencies, which are crucial for accurately capturing the long-range spatial dependencies that characterize phase separation dynamics (see ‘Fourier attention layer for universal approximation of differential operators’ in **Methods**). Together, these architectural innovations enable HPE-AFNO to accurately model complex spatiotemporal dynamics, even under sparse and noisy observational conditions (see **Discussion**), and to perform superior long-term spatiotemporal dynamics prediction.

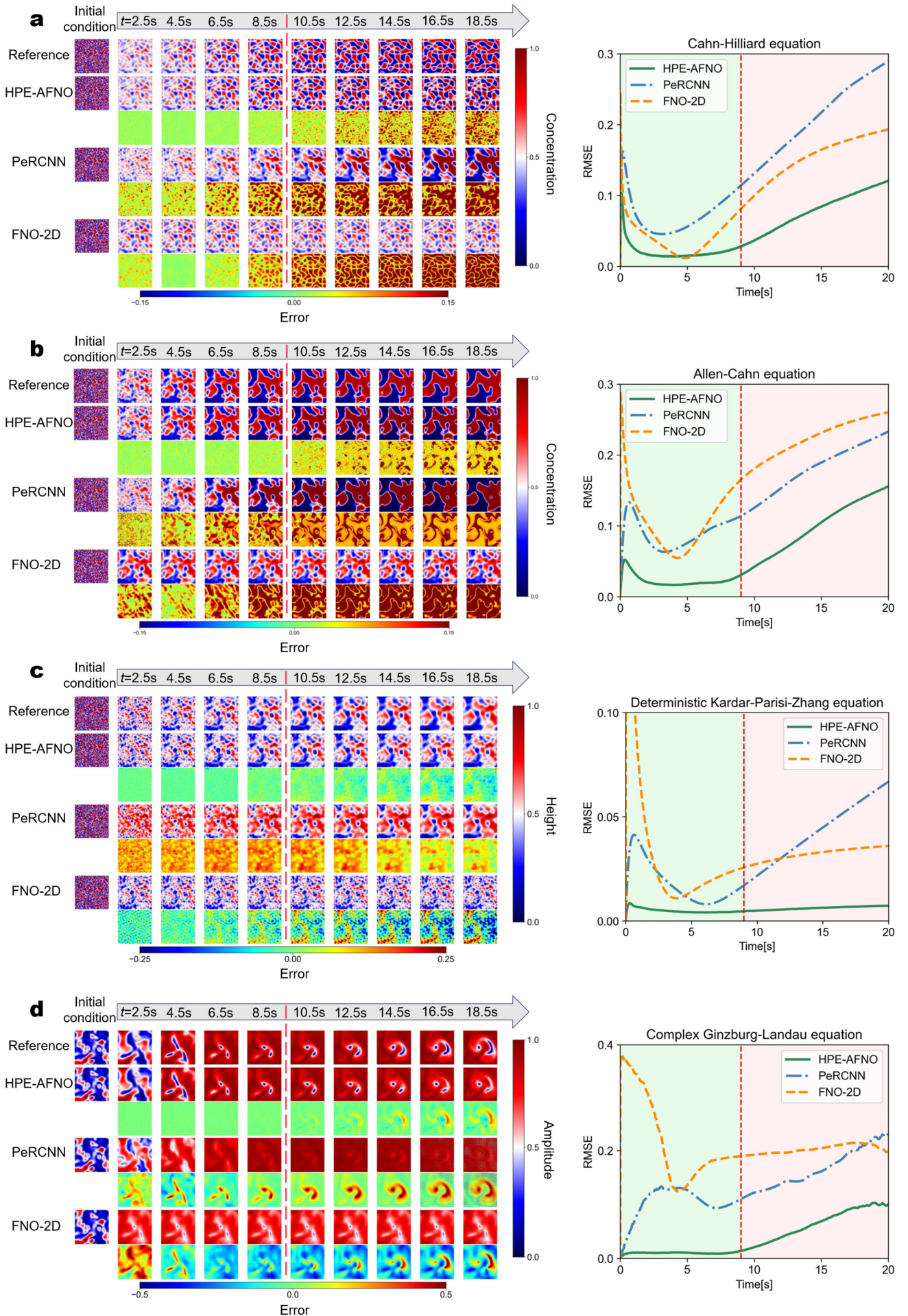


Fig. 2 | Comparative performance of HPE-AFNO and baseline models on four canonical PDE dynamics. **a–d**, Spatiotemporal prediction results for the (a) Cahn–Hilliard, (b) Allen–Cahn, (c) deterministic Kardar–Parisi–Zhang, and (d) complex Ginzburg–Landau equations. For each system, ground truth (top row) is compared with predictions from HPE-AFNO, PeRCNN, and FNO-2D, followed by corresponding error maps (bottom rows). The right panel in each subfigure shows the performance (RMSE) of spatiotemporal dynamic prediction, with the red dashed line at $t = 9$ s indicating the boundary between the interpolation regime (green background) and the extrapolation regime (pink background). Across all systems, HPE-AFNO consistently outperforms baseline models, with the performance advantage becoming more pronounced during extrapolation.

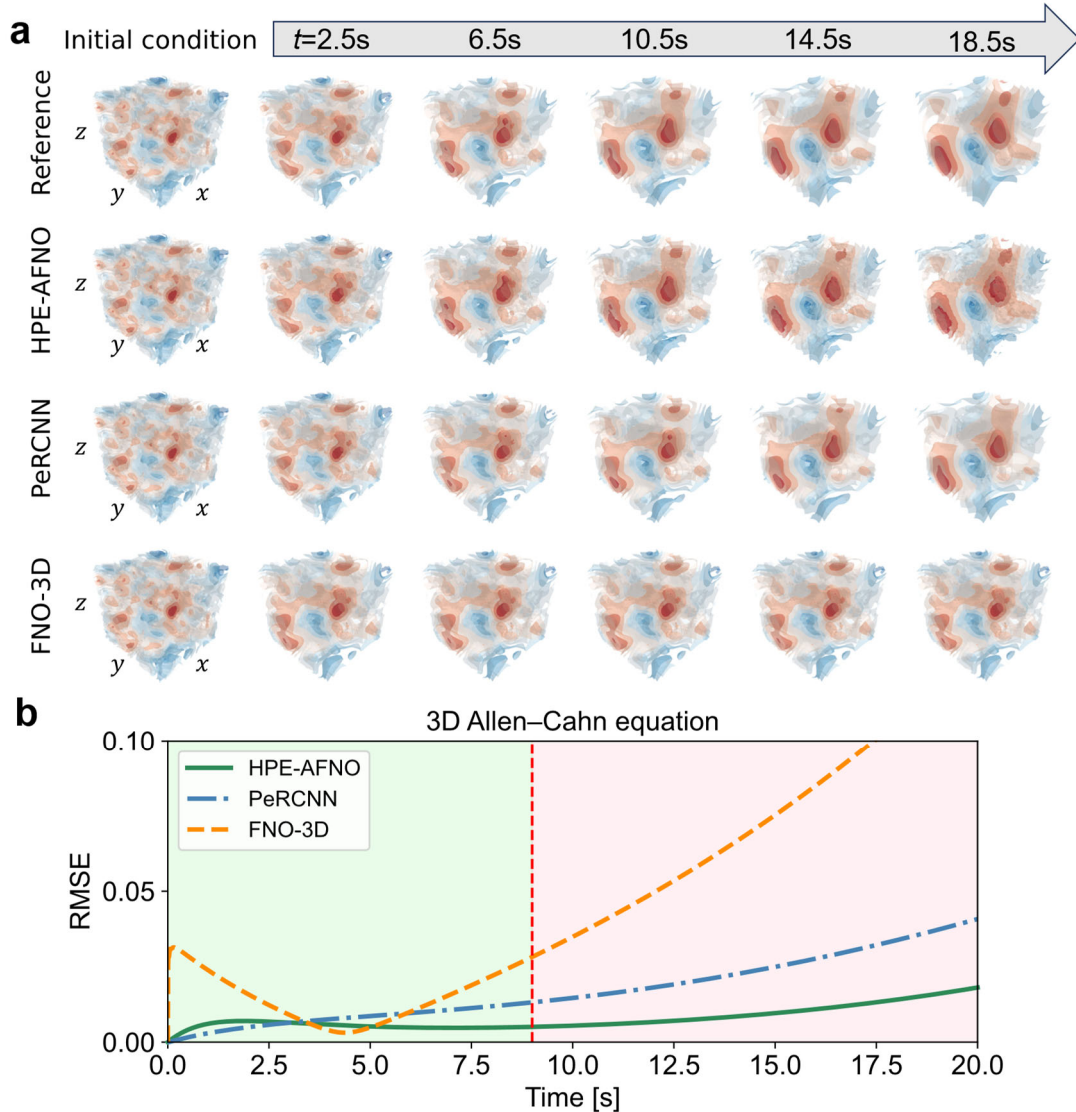


Fig. 3 | Comparative performance of HPE-AFNO and baseline models on the three-dimensional Allen–Cahn system. **a**, Spatiotemporal prediction results for the 3D-AC dynamics at representative time points. The ground truth (top row) is compared with predictions from HPE-AFNO, PeRCNN, and FNO-3D. Three-dimensional phase-field states are visualized using isosurfaces of the phase-field variable, highlighting the evolution of volumetric phase separation and interface structures over time. **b**, RMSE curves plotted over time for each model, showing performance during the interpolation phase (green-shaded background) and the extrapolation phase (pink-shaded background). The red dashed line indicates the transition point at $t = 9$ s between interpolation and extrapolation regimes.

(b) *Learning spatiotemporal dynamics from partial physics and data*

While our HPE-AFNO method excels at learning spatiotemporal dynamics from data where the underlying governing equations are entirely unknown, practical applications in complex systems, such as electrochemical modeling, often benefit significantly from the integration of partial physical insights. These insights typically manifest as known terms within PDEs. To evaluate the model’s ability to incorporate such partial information, we investigate two distinct scenarios:

(i) *White-black scenario*: In this case, the fundamental physical expressions (e.g., diffusion coefficients, reaction kinetics in an electrochemical system) are known, but their complex interactions and the overall combined form of the governing equations remain undetermined.

(ii) *Black-white scenario*: Conversely, this scenario assumes knowledge of the interaction patterns and combinatorial structure of the PDE is known, while the foundational physical expressions themselves are unknown and need to be learned from data.

These scenarios are benchmarked against a baseline *black-black* case, where neither the fundamental physical expressions nor their governing combinations are known. This comparative analysis serves to validate the model’s capacity to effectively embed and leverage existing physical knowledge.

As a representative example, we consider the CH equation, a model frequently employed in electrochemical and materials science and relevant to phase separation phenomena observed in battery electrodes:

$$\frac{\partial c}{\partial t} = \nabla \cdot (M(c) \nabla (\mu_{\text{hom}}(c) - \kappa \nabla^2 c)) \quad (1)$$

where $c(\mathbf{x}, t)$ is the conserved concentration field (e.g., of lithium ions), with \mathbf{x} and t representing spatial coordinates and time, respectively. The mobility function $M(c)$ is defined as the product of concentration c and concentration-dependent diffusivity $D(c)$. The chemical potential comprises two components: $\mu_{\text{hom}}(c)$, representing the homogeneous (bulk) contribution, and a gradient energy term $-\kappa \nabla^2 c$, where ∇ is the spatial gradient operator. The parameter κ is a positive constant known as the gradient energy coefficient. This gradient term is crucial as it accounts for interfacial energy contributions, resulting in the formation of diffuse interfaces between distinct phases (e.g., lithium-rich and lithium-poor phases) rather than infinitely sharp boundaries⁵¹. In this work, and consistent with previous studies^{13,51}, the homogeneous chemical potential and diffusivity are specifically defined as $\mu_{\text{hom}}(c) = \log c(1 - c)^{-1} + 3(1 - 2c)$ and $D(c) = (1 - c)$, respectively.

Our approach utilizes a hierarchical architecture that partitions the governing equation (1) into two segments. Two-level hierarchical modules are then employed to learn the spatiotemporal features

for each segment, as depicted in **Fig. 1a**. The first level focuses on learning the fundamental physical expressions (corresponding to the red-highlighted portion of the equation (1)), while the second level is designed to capture how these learned or known expressions interact and combine (corresponding to the green-highlighted portion). Each level consists of an AFNO module and a complementary pathway that directly incorporates known physical information. This structure facilitates the integration of learned representations with embedded physical insights. For instance, in the white-black scenario, terms like $M(c)$, $\mu_{\text{hom}}(c)$, and $\kappa\nabla^2 c$ are considered known, but their operational interactions within the PDE (e.g., products, sums, differential operators acting upon them) remain unspecified and are learned by the model.

Fig. 4 presents a comprehensive comparison of the three scenarios (black-black, white-black, black-white) using qualitative visualizations of the predicted spatiotemporal dynamics and quantitative error metrics (RMSE) by the utilization of HPE-AFNO. While all scenarios show comparable performance during the interpolation phase, significant divergences emerge in the extrapolation regime (defined as $t > 9\text{s}$ and highlighted by the pink-shaded background in **Fig. 4b**). Notably, for the black-black scenario, where the predicted spatiotemporal dynamics are learned entirely from data, the model exhibits the most substantial error accumulation over time during extrapolation. In contrast, both scenarios that embed partial physical knowledge (white-black and black-white) maintain significantly higher prediction accuracy in this challenging regime (**Fig. 4b**). Quantitatively, the average RMSE during extrapolation is reduced by 23.7% for the white-black scenario and 17.3% for the black-white scenario, relative to the black-black baseline. At a specific time point, $t = 15\text{s}$, the prediction error is reduced by 25% for the white-black and 18.5% for the black-white. These improvements underscore the model’s ability to leverage partial physical knowledge to enhance long-term predictive performance.

Interestingly, although the HPE-AFNO method has the highest error for the black-black scenario, it exhibits the lowest variance across multiple independent runs (**Fig. 4b**). This indicates that, without explicit physical guidance, the model tends to converge prematurely to a stable but inaccurate solution. In contrast, in the white-black and black-white scenarios, the variance is slightly higher, yet the learned spatiotemporal dynamics remain much closer to the ground truth. This moderate increase in variability reflects the model’s ability to adjust its predictions within a physically constrained solution space, enabling it to better capture the complexity of the dynamics without drifting away from physically plausible behavior. The performance gain is more substantial in the white-black case, indicating that providing known fundamental expressions (e.g., $M(c)$, $\mu_{\text{hom}}(c)$) is more effective in guiding the learning process than solely constraining their interactions.

The superior performance of HPE-AFNO in the white–black scenario can be attributed to two key architectural features. First, by explicitly embedding known physical components (such as $M(c)$, $\mu_{\text{hom}}(c)$, and $\kappa\nabla^2c$), the HPE-AFNO model benefits from physically grounded constraints. These constraints reduce the likelihood of learning implausible dynamics, particularly in the extrapolation regime where purely data-driven models are prone to significant error accumulation. Second, the model’s hierarchical design inherently mirrors the layered and compositional structure often found in physical laws. Instead of attempting to approximate the entire complex PDE operator in a single, monolithic stage, it first captures the structure of fundamental expressions and subsequently learns their interactions and nonlinear combinations. This modular decomposition simplifies the learning task, making training more tractable and improving data efficiency.

Beyond enhancing prediction performance, the embedding of partial physics also significantly improves model interpretability. This is a critical requirement when the goal is not just prediction but also the discovery of the underlying structure of partially known PDEs, which is important to scientific discovery and engineering design. This capability is further explored in the subsequent section, where we assess the model’s proficiency in discovering the complete structure of governing PDEs from such partially known formulations.

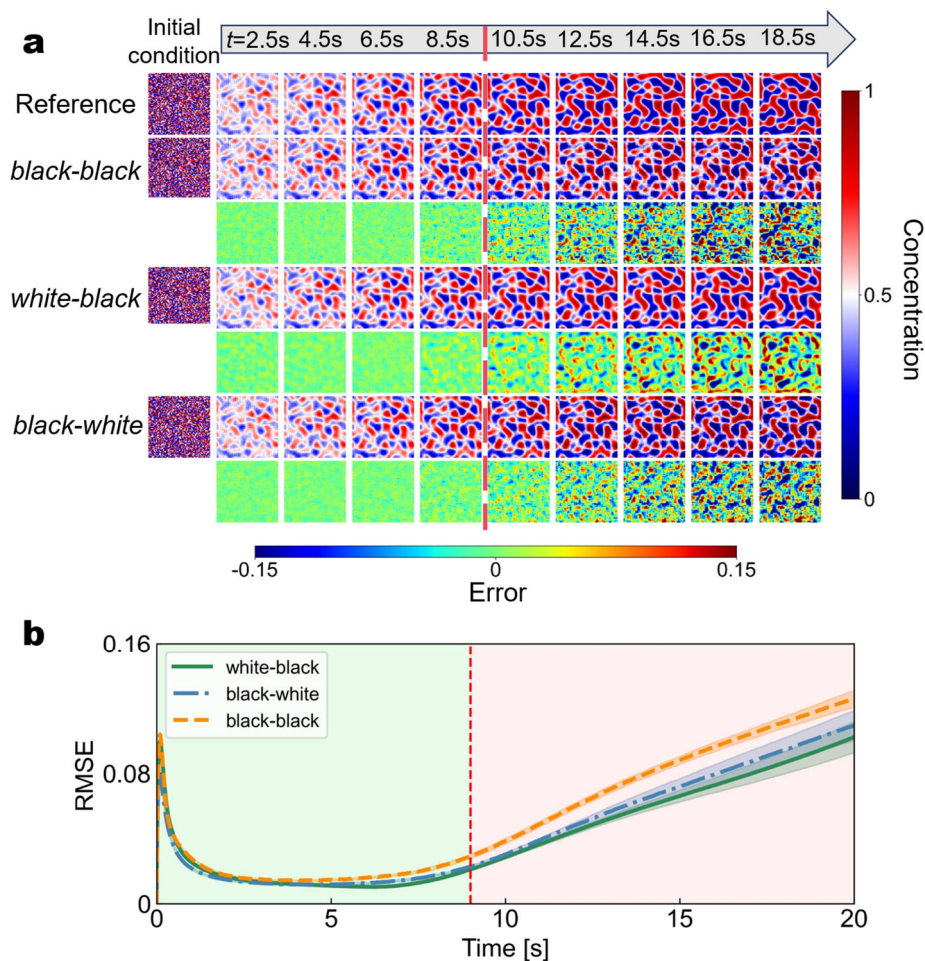


Fig. 4 | Comparative performance for the scenarios of black–black, white–black, and black–white, evaluated on the Cahn-Hilliard (CH) equation. **a**, Temporal evolution of predicted concentration fields from $t = 2.5$ s to 18.5 s. This panel compares the black–black (no physics incorporated), white–black (fundamental physical terms known, interactions unknown), and black–white (interactions known, fundamental terms unknown) scenarios against the ground truth simulation data. Corresponding error maps are displayed below each predicted field. Color bars indicate concentration values (right) and absolute error magnitudes (bottom). **b**, RMSE curves plotted over time for each scenario, showing model performance during the interpolation phase (green-shaded background) and the extrapolation phase (pink-shaded background). The red dashed line indicates the transition point at $t = 9$ s between interpolation and extrapolation regimes. Shaded regions around the curves represent the standard deviation calculated over five independent experimental runs.

2.2 Hierarchical physics-embedded learning for PDE discovery with limited and noisy data

Previous sections focused on scientific modeling tasks, such as data-driven or physics-embedded modeling, utilizing the proposed hierarchical framework. Numerical results demonstrated its excellent accuracy and extrapolation capabilities. However, the process of knowledge discovery extends beyond merely modeling the physical phenomena of interest. Crucially, translating learned data patterns—such as derived partial differential equations (PDEs) or empirical relationships—into understandable forms in terms of physical variables enables scientists to gain deeper insights and make reliable inferences about related problems. Therefore, this section extends the proposed hierarchical physics-embedded learning model to the task of discovering closed-form governing PDEs directly from data.

To formulate this task, let us reconsider the nonlinear system described by equation (1). The objective of equation discovery is to recover the closed-form governing PDEs, given only sparse and potentially noisy measurements of the system’s states. To achieve this, we integrate deep symbolic regression (DSR)⁵² techniques with our HPE-AFNO model. The proposed framework for PDE discovery is illustrated in **Fig. 5**, using the Cahn-Hilliard (CH) equation as an example. The procedure comprises three main steps: (1) Spatiotemporal dynamics prediction using the HPE-AFNO model, (2) concentration binning analysis for extracting functional dependencies, and (3) deep symbolic regression for identifying explicit mathematical expressions. These steps are detailed in ‘Equation discovery’ in **Methods** section.

We validate the effectiveness of our method by performing equation discovery on synthetic datasets generated from the CH equation, specifically focusing on scenarios characterized by sparse and noisy measurement data. As depicted in **Fig. 1a**, the proposed framework can learn fundamental physical expressions, as well as their governing interactions and combinations, by utilizing spatiotemporal features from either the first or second hierarchical level. In this case study, we assume the general form of the CH equation (equation (1)) was known, but the specific symbolic forms for the concentration-dependent diffusivity $D(c)$ and the homogeneous chemical potential $\mu_{\text{hom}}(c)$ are

unknown. We embedded known physical information (the known parts of the CH equation form) into the HPE-AFNO framework to reconstruct the spatiotemporal dynamics (**Fig. 5**). To ensure that the learned symbolic expressions represent physically meaningful continuous functions of the concentration field, we enforced functional consistency through strict constraints using a kernel-based mapping that mathematically guarantees that the predicted unknown terms exhibit continuous dependence on the input variable, such that locations with similar input values inherently receive similar weighting patterns from the kernel matrix and thus result in similar final encoded features (see **Methods**). Following the reconstruction phase, concentration binning analysis was employed to extract insights into the fundamental symbolic relationships learned by the network (**Fig. 5**). Subsequently, deep symbolic regression (see **Methods**) was performed to complete the equation discovery task without pre-supposing specific functional forms. Finally, the performance of our method was assessed by comparing both the statistical forms of the unknown terms (derived from concentration binning) and the explicit symbolic expressions (obtained via DSR) against the ground truth equations. Technical details of the framework are provided in the **Methods** section.

The results show that our method successfully recovers the complete governing PDEs when applied to sparse, noisy measurement data. Even with the noise level (see **Supplementary Note 4**) increased to 10% (**Supplementary Fig. 1** and **Supplementary Fig. 2**), our approach maintains competitive performance, accurately identifying both the mathematic expressions for diffusivity $D(c)$ and homogeneous chemical potential $\mu_{\text{hom}}(c)$ within the PDEs. In contrast, comparative methods—such as PeRCNN with sparse regression and end-to-end approaches like DSR and genetic programming—failed to identify the mathematical forms for either $D(c)$ or $\mu_{\text{hom}}(c)$. A detailed comparative analysis is provided in **Supplementary Note 5**, which demonstrates that our hierarchical approach consistently outperforms these baselines, particularly under challenging conditions involving sparse and noisy measurements.

This improvement stems from two key advantages of our framework. First, by embedding physical information within the HPE-AFNO architecture, our method enables accurate reconstruction of the full spatiotemporal dynamics from sparse observational data. In contrast, end-to-end approaches such as DSR typically require densely and continuously sampled time series to produce meaningful results, as they rely on explicit estimation of temporal derivatives from data and lack mechanisms to infer missing dynamics or incorporate prior physical knowledge. Second, our framework facilitates the decoupled identification of multiple coupled physical terms by structurally assigning each AFNO channel to a distinct unknown component. This architectural design enables each physical term to be identified independently and subsequently expressed as a symbolic equation, thereby simplifying the

overall equation discovery process and improving interpretability. By comparison, methods such as PeRCNN first reconstruct the complete spatiotemporal dynamics and then apply simultaneous sparse regression to identify all physical terms. This design increases sensitivity to reconstruction errors, which inevitably propagate into the regression stage and reduce the accuracy and reliability of the discovered equations. Furthermore, traditional sparse regression techniques are constrained by the use of predefined symbolic libraries, limiting their ability to recover non-polynomial or compositional expressions (see **Supplementary Note 5**).

In summary, these results underscore the effectiveness of our proposed hierarchical physics-embedded learning approach for tackling PDE discovery problems, particularly when dealing with the challenging conditions of sparse and noisy measurements.

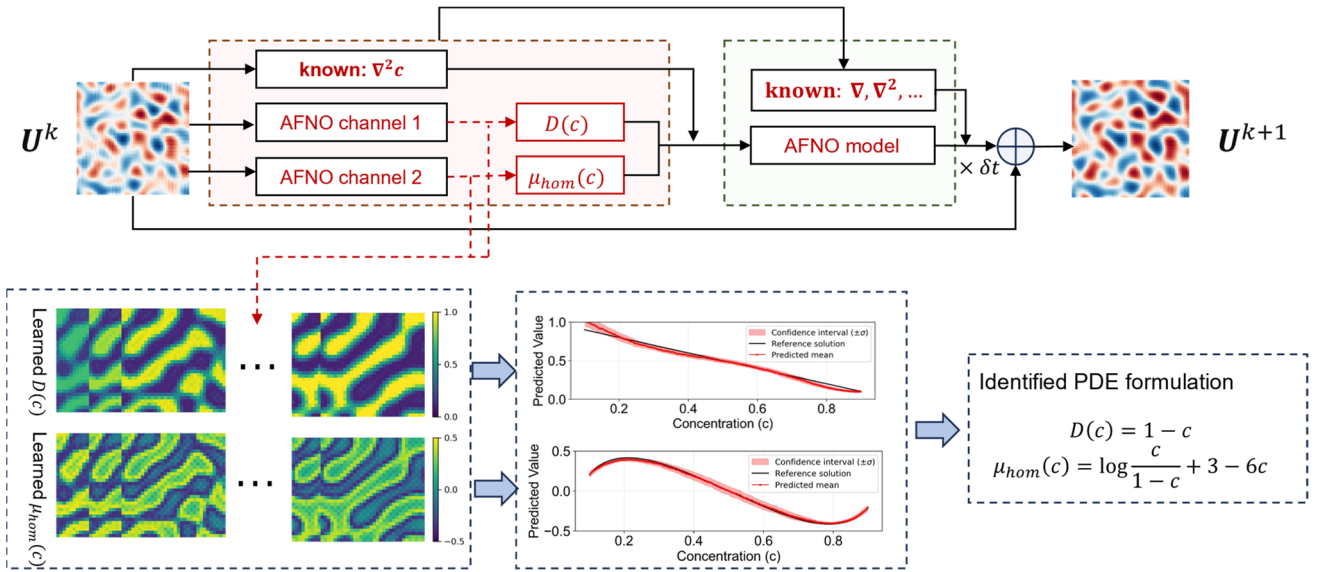


Fig. 5 | Framework for discovering closed-form PDEs using hierarchical physics-embedded learning. The procedure begins with the reconstruction of spatiotemporal dynamics from sparse and noisy measurements using the HPE-AFNO model. In the first level, two separate AFNO channels are used to learn the unknown physical terms: the concentration-dependent diffusivity $D(c)$ and the homogeneous chemical potential $\mu_{hom}(c)$, respectively. The second level embeds known physical operators, such as ∇^2 , to produce the next-step system's state U^{k+1} . To extract interpretable physical relationships, the predicted concentration field is subjected to binning analysis, which reveals the underlying functional dependencies without assuming specific forms. Finally, deep symbolic regression is applied to recover closed-form expressions of the unknown terms, enabling full equation discovery under sparse and noisy data conditions. This process is illustrated here using the CH equation as an example.

3 Discussion

To evaluate the practical performance of our physics-embedded modeling framework, we examine its performance under two common forms of data degradation: sparse temporal sampling and noise contamination. These conditions frequently arise in real-world PDE modeling due to limitations in

observation frequency and measurement accuracy³⁸. Using the CH and AC equations as two representative systems, we assess how well the HPE-AFNO framework maintains predictive accuracy when subjected to progressively sparser temporal sampling intervals and increasing levels of noise. Each experimental configuration is repeated five times with different random initial conditions to ensure statistical reliability.

Fig. 6 presents contour plots of the average RMSE, computed separately for interpolation and extrapolation tasks, over a two-dimensional input space defined by sampling interval (δt) and noise level. For the CH system (**Fig. 6a**), the interpolation regime (left panel) demonstrates strong predictive robustness: the average RMSE increases only slightly under extremely sparse sampling and high noise, indicating that the model successfully reconstructs the full spatiotemporal dynamics within the interpolation window even when the input data are heavily degraded. In the extrapolation regime (right panel), RMSE increases more noticeably, but predictive accuracy remains high overall. Notably, the majority of this increase occurs between $\delta t = 0.4s$ and $0.8s$, suggesting that the model retains high reliability until extreme sparsity is introduced. Even so, prediction errors remain well controlled, and no abrupt degradation in performance is observed.

This adaptability to temporal sparsity and noise contamination arises from the interplay between the model’s recursive prediction strategy and its hierarchical physics-embedded architecture. The recursive mechanism enables long-range forecasts to be constructed from a sequence of short-step transitions, allowing the model to progressively infer intermediate states even when large portions of the input sequence are missing. This approach effectively bridges the temporal gaps induced by sparse observations and mitigates error accumulation during extrapolation. Meanwhile, the hierarchical physics-embedded structure imposes physically meaningful constraints on the learned dynamics, regularizing predictions and suppressing nonphysical deviations introduced by noisy inputs. Quantitative analysis confirms that even under a noise level of 20% and an 80-fold reduction in sampling frequency (corresponding to a fully resolved interval of 0.01s), the framework maintains accurate and stable long-term predictions. Similar trends are observed for the AC system (**Fig. 6b**), further underscoring the robustness of HPE-AFNO in the presence of sparse and noisy input data.

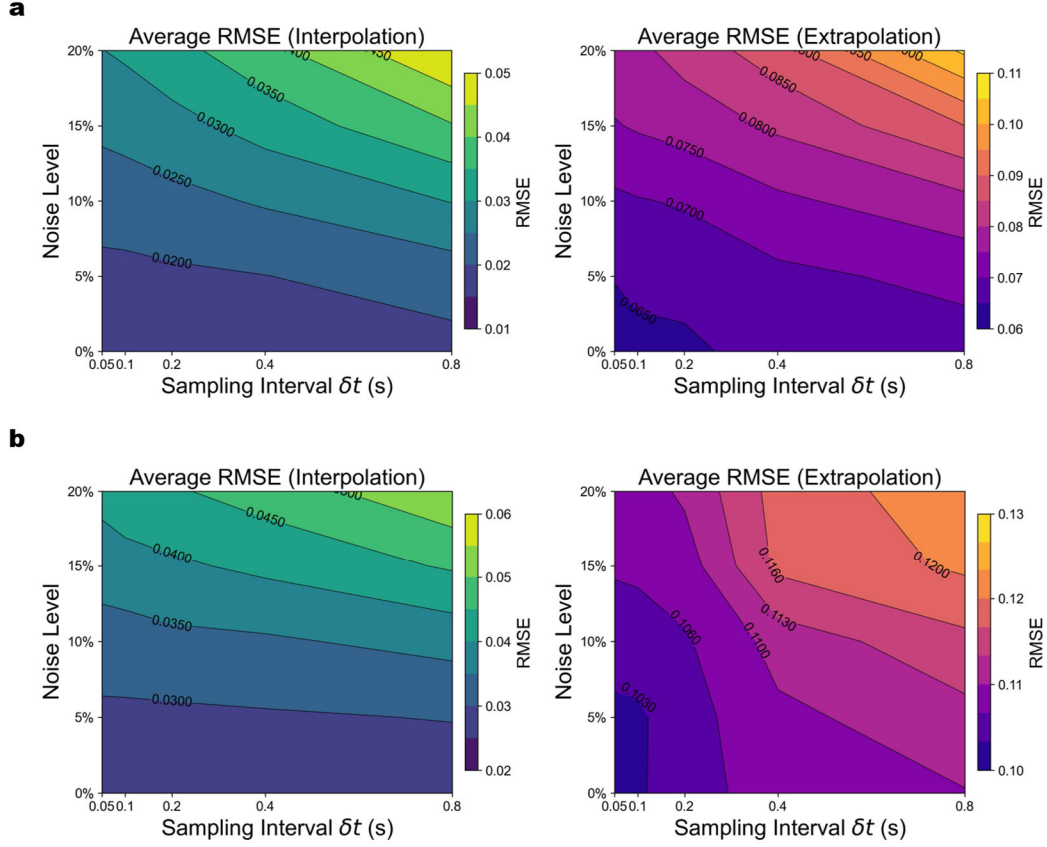


Fig. 6 | Robustness of HPE-AFNO to data sparsity and noise contamination in phase-separation PDE systems. a, Cahn–Hilliard system; **b,** Allen–Cahn system. Each panel presents contour plots of the average RMSE computed separately for interpolation (left) and extrapolation (right) regions across a two-dimensional input space defined by the temporal sampling interval (δt) and noise level. RMSE values are averaged over five independent runs with distinct random initial conditions. Across both systems, the model exhibits strong robustness to temporal sparsity and noise, with only limited increases in prediction error, indicating strong robustness in both interpolation and extrapolation regimes.

4 Conclusions

This work introduces a hierarchical physics-embedded framework, HPE-AFNO, for modeling and discovery of complex spatiotemporal systems governed by PDEs, particularly in scenarios where physical knowledge is incomplete. The core advantage of HPE-AFNO lies in its two-level hierarchical architecture, which mirrors the process of discovering physical laws: the first level uses adaptive Fourier neural operators to extract fundamental symbolic expressions by capturing global dependencies, while the second level models the complex interactions and governing combinations among these expressions. This decomposition simplifies learning by reducing the order of differential operators required at each stage and by explicitly modeling the nonlinear combinations among symbolic components, which together enable the model to effectively handle systems with high-order differential operators and strong nonlinear terms. Through extensive numerical experiments, we

demonstrate the effectiveness of HPE-AFNO in forward modeling tasks across various representative PDE systems. Compared to several baseline models, the proposed framework exhibits strong extrapolation ability and robustness to sparse and noisy data. Using the Cahn–Hilliard equation as a representative example, HPE-AFNO achieves a 71.2% reduction in RMSE during interpolation and a 62.8% reduction during extrapolation compared to PeRCNN. It also outperforms FNO-2D by 51.3% and 49.2%, respectively. In addition, the framework flexibly embeds known physical laws through dedicated computational channels, bypassing the need to learn established terms and directly incorporating them into the model. This structural embedding ensures physical consistency while substantially improving long-term predictive accuracy and interpretability. For instance, in the white–black scenario where partial physics is embedded, the average RMSE during extrapolation is reduced by 23.7% compared to the baseline without physical guidance.

Equally important, HPE-AFNO enables the discovery of explicit mathematical forms of unknown physical terms by seamlessly integrating with deep symbolic regression. By structurally separating known and unknown components, the framework extracts the outputs corresponding to unknown terms after training, which are then passed to a symbolic regression module. This design overcomes key limitations of traditional methods by allowing the identification of diverse mathematical expressions without relying on prior structural assumptions. On the Cahn–Hilliard system, where the forms of diffusivity $D(c)$ and chemical potential $\mu_{hom}(c)$ are unknown, HPE-AFNO successfully recovers both expressions. In contrast, baseline approaches such as PeRCNN combined with sparse regression and end-to-end symbolic methods like deep symbolic regression fail to identify either term under the same conditions. These results highlight the potential of HPE-AFNO as a general framework for discovering governing equations from incomplete and noisy data.

Together, these results establish HPE-AFNO as a versatile and interpretable framework for modeling and discovery in complex dynamical systems governed by PDEs. Its modular architecture, physical interpretability, and ability to incorporate partial prior knowledge make it broadly applicable across diverse PDE-driven systems. Beyond the benchmark cases investigated in this work, HPE-AFNO can be extended to more challenging scenarios involving multi-physics coupling, irregular spatial geometries, and real-world experimental data. As scientific applications increasingly demand modeling approaches that are accurate, data-efficient, and physically consistent, HPE-AFNO offers a promising foundation for advancing both predictive modeling and equation discovery in systems with incomplete or partially known physical laws.

5 Methods

5.1 HPE-AFNO framework

Consider a spatiotemporal dynamical system whose spatiotemporal evolution is governed by a partial differential equation (PDE) with high-order differential terms and nonlinear operators:

$$\mathbf{u}_t = \mathcal{F}(\mathbf{u}, \mathbf{u}_x, \mathbf{u}_{xx}, \mathbf{u}_{xxx}, \mathbf{u}_{xxxx}, \dots, \mathbf{x}, t) \quad (2)$$

where $\mathbf{u}(\mathbf{x}, t) \in \mathbb{R}^n$ represents the state variable—namely, the observational data or snapshots collected from experiments or nature—with (\mathbf{x}, t) ranging over the space–time domain $\Omega \times T$. \mathbf{u}_x and \mathbf{u}_{xx} denotes the first-order and second-order spatial derivative regarding the spatial variable \mathbf{x} respectively, and the same convention applies to higher-order derivatives; \mathbf{u}_t represents the first-order time derivative; and \mathcal{F} is a nonlinear function involving \mathbf{u} and its spatial derivatives of various orders with nonlinear operators such as logarithmic functions. The solution is specified together with $\mathcal{I}(\mathbf{u}; t = 0, \mathbf{x} \in \Omega) = 0$ and $\mathcal{B}(\mathbf{u}; \mathbf{x} \in \partial\Omega) = 0$ as the initial and boundary conditions, respectively.

Through numerical discretization with time step δt , we reformulate this PDE using a forward Euler scheme, enabling the construction of a spatiotemporal learning model where the state variable \mathbf{u} is updated via a recurrent network with shared parameters:

$$\hat{\mathbf{u}}^{k+1} = \hat{\mathbf{u}}^k + \hat{\mathcal{F}}(\hat{\mathbf{u}}^k, \theta) \delta t \quad (3)$$

where, $\hat{\mathbf{u}}^k$ represents the prediction at time t_k , and $\hat{\mathcal{F}}$ is an approximation of \mathcal{F} parameterized by θ . The approximation functions as a proxy for a series of operations responsible for calculating the first-order time derivative as specified in equation (2).

A key challenge in this framework is developing an autoregressive neural network capable of accurately learning \mathcal{F} through frame-by-frame prediction, ensuring robust recursive updates of the state variable $\mathbf{U}^k \in \mathbb{R}^{H \times W}$ (In this work we mainly study two-dimensional cases). We introduce a hierarchical architecture that mirrors the progressive discovery process of physical laws (as shown in Fig.1). Specifically, we implement a two-level architecture: the first-level for extracting fundamental physical terms and the second-level for learning the governing interactions and combinations among these fundamental terms. Take the CH equation as an illustrative example, where the state variable is the concentration c (i.e. $u = c$). The first level specializes in extracting spatiotemporal features corresponding to constitutive relations with respect to c (i.e., the product of concentration and concentration-dependent diffusivity $M(c)$, the homogeneous chemical potential $\mu_{\text{hom}}(c)$, and the gradient energy term $-\kappa \nabla^2 c$, where ∇ denotes the spatial gradient). To achieve this, we employ an

attention layer based on a Fourier mixer^{40,41} that leverages the powerful expressiveness of vision transformers. The Fourier layer $\mathbf{Y}^k = \text{FourierLayer}(\mathbf{U}^k)$ consists of three parts: (1) employ the discrete Fourier transform to mix different tokens: $\mathbf{Z}^k[i, j, :] = \text{DFT}(\bar{\mathbf{U}}^k)[i, j, :]$ where $\bar{\mathbf{U}}^k \in \mathbb{R}^{H' \times W' \times d}$ is obtained through patch and position embedding from the input \mathbf{U}^k ; (2) multiply the weight matrix $\mathbf{W}_f \in \mathbb{C}^{H' \times W' \times d \times d}$ in the frequency domain to mix different channels: $\bar{\mathbf{Z}}^k[i, j, :] = \mathbf{W}_f[i, j, :, :] \mathbf{Z}^k[i, j, :]$; and (3) adopt the inverse discrete Fourier transform: $\mathbf{Y}^k[i, j] = \text{IDFT}(\bar{\mathbf{Z}}^k)[i, j]$. To further reduce the number of learnable parameters and improve the adaptability, the multilayer perceptron (MLP) with shared parameters is adopted in step (2): $\bar{\mathbf{Z}}^k[i, j, :] = \mathbf{W}_{f2} \sigma(\mathbf{W}_{f1} \mathbf{Z}^k[i, j, :]) + \mathbf{b}$ ^{40,41}. This layer excels at capturing global dependencies between inputs and outputs through frequency-domain learning, especially in modeling complex nonlinear (e.g., non-polynomial) operators compared to CNN-based methods that rely on local convolutional kernels. We prove that this Fourier attention layer can approximate any differential operator (see ‘Fourier attention layer for universal approximation of differential operators’ for detailed information). For multi-feature outputs, we modify the first-level AFNO module to generate multiple channels that feed into the second-level combination learning. The second level learns the complex interactions and combinations between $M(c)$, $\mu_{\text{hom}}(c)$ and $-\kappa \nabla^2 c$ (i.e., $\nabla \cdot (M(c) \nabla (\mu_{\text{hom}}(c) - \kappa \nabla^2 c))$). We utilize the same Fourier attention layer as the first-level. This hierarchical design significantly reduces learning complexity through decomposition (particularly by lowering the order of differential operators required at each level).

Moreover, it enables more direct and flexible embedding of known physical constraints compared to previous approaches like PeRCNN. For a known fundamental physical term, we can create a separate embedding channel to directly compute and fuse it with other output in the first-level. For example, if we know $\mu_{\text{hom}}(c) = \log c(1 - c)^{-1} + 3(1 - 2c)$, we can directly calculate this term in a separate channel and feed it with the outputs of the Fourier attention channels (corresponding to the unknown terms $M(c)$ and $-\kappa \nabla^2 c$) into the second-level learning. For known governing interactions and combinations, we utilize the outputs of the Fourier attention channels in the first-level as the corresponding unknown physical terms, and the results of the separate embedding channels as the corresponding known terms. With these fundamental terms, we can form a separate embedding channel in the second-level to compute the results following these known combinations. This structured embedding enforces physical consistency in predictions, substantially enhancing both predictive accuracy for long-term dynamics and physical interpretability. This superiority is demonstrated by the numerical experiments. In summary, physics-embedding channels enforce known physical laws, while

Fourier attention channels model the residual (potentially complex) dynamics at both levels.

5.2 Hierarchical error decomposition of HPE-AFNO

The key design of HPE-AFNO is to factorize \mathcal{F} into a two-level hierarchy that reduces learning complexity and provides a direct pathway for embedding prior physical knowledge. This design yields a transparent decomposition of the approximation error $\|\hat{\mathcal{F}} - \mathcal{F}\|$ into two components: (i) the first-level error in extracting fundamental physical terms, and (ii) the second-level error in learning how to combine these terms into the governing equations. To formalize this decomposition precisely, we adopt the following assumptions:

Assumption 1. \mathcal{F} can be expressed as the composition of an ideal extractor and an ideal combiner:

$$\mathcal{F}(\mathbf{u}) = \mathcal{C}(\mathcal{E}(\mathbf{u})), \quad \forall \mathbf{u} \in \Omega_{\mathbf{u}}, \quad (4)$$

where $\mathcal{E}(\cdot) = (\mathcal{E}_1(\cdot), \dots, \mathcal{E}_m(\cdot))$ denotes m fundamental physical terms, $\mathcal{C}(\cdot)$ denotes the rule that combines these terms into the time derivative, and $\Omega_{\mathbf{u}}$ denotes the domain of \mathbf{u} . Accordingly, our HPE-AFNO model can be represented as:

$$\hat{\mathcal{F}}(\mathbf{u}, \theta) = \hat{\mathcal{C}}(\hat{\mathcal{E}}(\mathbf{u}, \theta_{\hat{\mathcal{E}}}), \theta_{\hat{\mathcal{C}}}), \quad (5)$$

where $\hat{\mathcal{E}}(\cdot) = (\hat{\mathcal{E}}_1(\cdot), \dots, \hat{\mathcal{E}}_m(\cdot))$ denotes the approximation of $\mathcal{E}(\cdot)$ parameterized by $\theta_{\hat{\mathcal{E}}}$, $\hat{\mathcal{C}}(\cdot)$ denotes the approximation of $\mathcal{C}(\cdot)$ parameterized by $\theta_{\hat{\mathcal{C}}}$, and $\theta = (\theta_{\hat{\mathcal{E}}}, \theta_{\hat{\mathcal{C}}})$.

Assumption 2. $\hat{\mathcal{C}}$ is Lipschitz continuous with respect to its feature input under $\|\cdot\|_2$; that is, there exists $L_{\hat{\mathcal{C}}} > 0$ such that for any $\mathbf{z}_1, \mathbf{z}_2$:

$$\|\hat{\mathcal{C}}(\mathbf{z}_1, \theta_{\hat{\mathcal{C}}}) - \hat{\mathcal{C}}(\mathbf{z}_2, \theta_{\hat{\mathcal{C}}})\|_2 \leq L_{\hat{\mathcal{C}}} \|\mathbf{z}_1 - \mathbf{z}_2\|_2. \quad (6)$$

To quantify the two-level approximation implied by this factorization, we define three complementary error measures on the state variable region $\Omega_{\mathbf{u}}$. First, for each extracted feature channel, we measure its worst-case deviation from the corresponding ideal term by:

$$\epsilon_{\mathcal{E}_i} = \sup_{\mathbf{u} \in \Omega_{\mathbf{u}}} \|\hat{\mathcal{E}}_i(\mathbf{u}, \theta_{\hat{\mathcal{E}}}) - \mathcal{E}_i(\mathbf{u})\|_2, \quad i = 1, \dots, m, \quad (7)$$

which summarizes the first-level extraction error across $\Omega_{\mathbf{u}}$. Second, we quantify the error of the second-level model in learning the governing combination rule, evaluated on the ideal feature inputs $\mathcal{E}(\mathbf{u})$:

$$\epsilon_c = \sup_{\mathbf{u} \in \Omega_u} \|\hat{\mathcal{C}}(\mathcal{E}(\mathbf{u}), \theta_{\hat{c}}) - \mathcal{C}(\mathcal{E}(\mathbf{u}))\|_2. \quad (8)$$

This term isolates the combination error from feature extraction, and reflects how accurately the model maps physical features to the time derivative once the correct components are provided. Finally, to connect the hierarchical analysis to the learning objective, we define the overall approximation error as:

$$\epsilon = \sup_{\mathbf{u} \in \Omega_u} \|\hat{\mathcal{F}}(\mathbf{u}, \theta) - \mathcal{F}(\mathbf{u})\|_2. \quad (9)$$

Together, $\{\epsilon_{\mathcal{E}_i}\}_{i=1}^m$, ϵ_c , and ϵ provide an interpretable accounting of model error: $\{\epsilon_{\mathcal{E}_i}\}_{i=1}^m$ characterizes the error when extracting fundamental physical terms, ϵ_c captures deviations in their governing composition, and ϵ measures the resulting overall discrepancy in the induced dynamics.

With these quantities, we can relate the end-to-end mismatch to the two-level hierarchy. In particular, the overall approximation error can be upper bounded by a sum of two terms: the aggregated feature extraction errors $\{\epsilon_{\mathcal{E}_i}\}_{i=1}^m$ from the first level, scaled by the Lipschitz constant of the combiner, and the combination error ϵ_c evaluated on ideal features from the second-level:

Theorem 1. *Under Assumptions 1 and 2, the overall error admits the following decomposition-bound:*

$$\epsilon \leq \epsilon_c + L_{\hat{c}} \left(\sum_{i=1}^m \epsilon_{\mathcal{E}_i}^2 \right)^{\frac{1}{2}}. \quad (10)$$

Proof. By Assumption 1, for any $\mathbf{u} \in \Omega_u$, we have:

$$\begin{aligned} \|\hat{\mathcal{F}}(\mathbf{u}, \theta) - \mathcal{F}(\mathbf{u})\|_2 &= \|\hat{\mathcal{C}}(\hat{\mathcal{E}}(\mathbf{u}, \theta_{\hat{\mathcal{E}}}), \theta_{\hat{c}}) - \mathcal{C}(\mathcal{E}(\mathbf{u}))\|_2 \\ &\leq \|\hat{\mathcal{C}}(\hat{\mathcal{E}}(\mathbf{u}, \theta_{\hat{\mathcal{E}}}), \theta_{\hat{c}}) - \hat{\mathcal{C}}(\mathcal{E}(\mathbf{u}))\|_2 + \|\hat{\mathcal{C}}(\mathcal{E}(\mathbf{u})) - \mathcal{C}(\mathcal{E}(\mathbf{u}))\|_2. \end{aligned} \quad (11)$$

For the first term in equation (11), Assumption 2 implies:

$$\begin{aligned} \|\hat{\mathcal{C}}(\hat{\mathcal{E}}(\mathbf{u}, \theta_{\hat{\mathcal{E}}}), \theta_{\hat{c}}) - \hat{\mathcal{C}}(\mathcal{E}(\mathbf{u}))\|_2 &\leq L_{\hat{c}} \|\hat{\mathcal{E}}(\mathbf{u}, \theta_{\hat{\mathcal{E}}}) - \mathcal{E}(\mathbf{u})\|_2 \\ &= L_{\hat{c}} \left(\sum_{i=1}^m \|\hat{\mathcal{E}}_i(\mathbf{u}, \theta_{\hat{\mathcal{E}}}) - \mathcal{E}_i(\mathbf{u})\|_2^2 \right)^{\frac{1}{2}}. \end{aligned} \quad (12)$$

For the definition of $\epsilon_{\mathcal{E}_i}$ and ϵ_c in equation (7) – (8), we have $L_{\hat{c}} \left(\sum_{i=1}^m \|\hat{\mathcal{E}}_i(\mathbf{u}, \theta_{\hat{\mathcal{E}}}) - \mathcal{E}_i(\mathbf{u})\|_2^2 \right)^{\frac{1}{2}} \leq$

$L_{\hat{\mathcal{C}}}(\sum_{i=1}^m \epsilon_{\hat{\mathcal{E}}_i}^2)^{\frac{1}{2}}$ and $\|\hat{\mathcal{C}}(\mathcal{E}(\mathbf{u})) - \mathcal{C}(\mathcal{E}(\mathbf{u}))\|_2 \leq \epsilon_{\mathcal{C}}$, respectively. Therefore, we have:

$$\|\hat{\mathcal{F}}(\mathbf{u}, \theta) - \mathcal{F}(\mathbf{u})\|_2 \leq L_{\hat{\mathcal{C}}} \left(\sum_{i=1}^m \epsilon_{\hat{\mathcal{E}}_i}^2 \right)^{\frac{1}{2}} + \epsilon_{\mathcal{C}}. \quad (13)$$

Taking the supremum of $\|\hat{\mathcal{F}}(\mathbf{u}, \theta) - \mathcal{F}(\mathbf{u})\|_2$ over $\mathbf{u} \in \Omega_u$ yields equation (10).

Theorem 1 yields an upper bound on the learning error for the hierarchical architecture: the overall mismatch is controlled by the residual error in the second-level combination and by the accumulated deviations in the extracted features, moderated by the Lipschitz constant $L_{\hat{\mathcal{C}}}$. This perspective also clarifies the practical advantage of physics embedding. Once a subset of physical terms is known and incorporated into the first level, the corresponding $\epsilon_{\hat{\mathcal{E}}_i}$ can be driven close to zero; similarly, if part of the combination rule is known and enforced in the second level, $\epsilon_{\mathcal{C}}$ is reduced to the remaining unknown interactions. In both cases, the bound in equation (10) tightens accordingly, leading to a smaller upper bound on the overall operator approximation error ϵ .

5.3 Equation discovery

The proposed methodology for discovering the governing partial differential equations, leveraging the HPE-AFNO model, comprises three steps: (1) spatiotemporal dynamics prediction, (2) concentration binning analysis, and (3) deep symbolic regression. These steps are detailed below.

Spatiotemporal dynamics prediction. A key challenge in data-driven PDE discovery is that the target physical terms (e.g., diffusivity coefficients, homogeneous chemical potential in phase-field processes) are often not directly measurable. Furthermore, experimentally accessible state variables, such as concentrations (c), are typically sparse and corrupted by noise. Therefore, a crucial initial step involves processing this raw, sparse data to reconstruct a high-fidelity, denoised representation of the system's dynamics, effectively inferring the behavior of the underlying, unmeasured physical terms.

Within our framework, the HPE-AFNO serves as this reconstruction model. This procedure adheres to the approach outlined previously in the 'HPE-AFNO framework' section. Specifically, we configure the HPE-AFNO model by embedding known fundamental physical operators (e.g., diffusion terms) into its first hierarchical level and known composite terms (e.g., combinations of derivatives) into the second level. This structured model is then trained using the available sparse measurements of the state variable u (i.e., concentration in this work).

Furthermore, a critical physical requirement is that the inferred unknown terms exhibit a

continuous functional dependence on the input state variable (concentration). To enforce this, we integrate a kernel-based feature mapping mechanism into the HPE-AFNO model tasked with learning these unknown physical terms. The underlying principle is that unknown physical terms or constitutive relations (e.g., diffusivity $D(c)$ or chemical potential $\mu(c)$) should yield similar values for similar input concentrations. This is achieved using a positive definite kernel function that quantifies similarity between input values. While various kernels are applicable, we utilize a Gaussian kernel⁵⁶ for its effectiveness and simplicity:

$$\kappa(u(i), u(j)) = \exp\left(-\frac{(u(i) - u(j))^2}{2\sigma^2}\right) \quad (14)$$

where $u(i)$ and $u(j)$ are input variable values (e.g., concentrations) at two different spatial locations, and σ is a hyperparameter controlling the characteristic length scale of similarity. The kernel κ assigns a similarity score approaching 1 for nearby input values, decaying towards 0 as the difference increases.

Normalized consistency weights w_{cons} are computed as $w_{\text{cons}} = \kappa / \sum(\kappa + \epsilon)$, where the summation is performed over all spatial locations and ϵ is a small constant ensuring numerical stability. The final encoded features representing the unknown physical term at each location are then calculated as a weighted average of the neural network's outputs across all spatial locations, using these similarity-based weights (w_{cons}). This kernel-based mapping mathematically guarantees that the predicted unknown terms exhibit continuous dependence on the input variable; locations with similar input values inherently receive similar weighting patterns from the kernel matrix, resulting in similar final encoded features.

Concentration binning analysis. Once the spatiotemporal dynamics are reconstructed by the HPE-AFNO, yielding reliable estimates of the unknown physical terms across space and time, the next step is to extract their functional dependence on the state variable (e.g., concentration c). Using the CH equation as an illustrative example, we aim to determine the explicit functional forms of terms like the concentration-dependent diffusivity $D(c)$ and the homogeneous chemical potential $\mu_{\text{hom}}(c)$. To achieve this, we employ a concentration binning analysis to the model's inferred values of these unknown terms. This process generates statistical representations that serve as input for the subsequent step of deep symbolic regression.

Specifically, the concentration range (typically normalized to $[0, 1]$) is divided into N uniform bins. For each bin i , corresponding to the concentration interval $[c_i, c_{i+1}]$, we collect all the model's predictions for a given unknown physical term, denoted $\zeta(c_x)$, where the local concentration c_x at

spatial location x falls within this interval. The average of these collected predictions ζ_i is then computed and associated with the midpoint concentration of the bin $(c_i + c_{i+1})/2$. Compiling these average values across all N bins yields a discretized representation of the unknown physical term as a function of concentration (e.g., **Fig. 4**).

This ensemble averaging within each concentration bin effectively smooths out stochasticity or fluctuations inherent in the neural network’s point-wise predictions. It robustly reveals the underlying functional relationship between the unknown physical term and the concentration variable, providing a high-quality data suitable for discovering interpretable mathematical expressions via deep symbolic regression.

Deep symbolic regression. Having obtained the statistical representations of the unknown physical terms via concentration binning analysis, we can identify potential functional relationships between these terms and the state variables (e.g., the concentration field in the CH equation). This facilitates the application of deep symbolic regression (DSR) to discover the explicit analytical structure of the underlying PDEs (e.g., the explicit equations for the diffusivity coefficient $D(c)$ and homogeneous chemical potential $\mu_{\text{hom}}(c)$).

DSR⁵² is a widely used technique for data-driven equation discovery that represents mathematical expressions as symbolic trees, which are then typically traversed sequentially. Specifically, DSR often utilizes a recurrent neural network (RNN) to probabilistically generate these expression trees token by token. Let τ denote the candidate expression. The i th token in the traversal is τ_i , selected from a predefined library \mathcal{L} of mathematical variables and operators (e.g., $\{+, -, \times, \div, \log, \exp\}$). The total length of the traversal is $|\tau| = T$.

The RNN, parameterized by ϕ , outputs a probability distribution $\psi^{(i)}$ at step i for selecting the i th token τ_i , conditioned on the preceding tokens $\tau_{1:(i-1)}$. This generative process continues until a complete expression tree is formed. The overall likelihood of sampling expression τ is given by the product of the probabilities of selecting each token:

$$p(\tau|\phi) = \prod_{i=1}^T p(\tau_i|\tau_{1:(i-1)}; \phi) = \prod_{i=1}^T \psi_{\mathcal{L}(\tau_i)}^{(i)} \quad (15)$$

Due to the non-differentiability of the reward function with respect to the RNN parameters ϕ , reinforcement learning (RL) is typically employed for training. In this RL framework, the distribution over expressions $p(\tau|\phi)$ represents the policy, the sequence of sampled tokens forms an action sequence (or episode), and a reward function evaluates the quality of the generated expression τ .

Notably, the total reward $R(\tau)$ is typically assigned based on the evaluation of the completed expression (e.g., its fit to the target data), rather than as a sum of time-discounted rewards for individual token selections.

To enhance the discovery of high-performing expressions, a risk-seeking policy gradient objective is adopted:

$$J_{risk}(\phi, \epsilon) = \mathbb{E}_{\tau \sim p(\tau|\phi)}[R(\tau)|R(\tau) \geq q_\epsilon(R)] \quad (16)$$

where the objective, characterized by the parameter ϵ ($0 < \epsilon \leq 1$), prioritizes maximizing rewards within the top ϵ quantile ($q_\epsilon(R)$) of the reward distribution.

As illustrated in **Fig. 4**, we establish potential functional relationships between the inferred unknown physical terms and the concentration field. Accordingly, the DSR reward function $R(\tau)$ quantifies the agreement between a candidate expression τ and the statistical data derived from the concentration binning analysis. This is typically achieved using a metric of normalized root-mean-square error (NRMSE): $R(\tau) = 1/(1 + \text{NRMSE})$. Compared to traditional equation discovery approaches reliant on sparse regression with predefined candidate libraries^{30,57}, this DSR-based method offers greater flexibility, as it does not necessitate *a priori* assumptions about the underlying equation's structure (further discussion in **Supplementary Note 5**).

5.4 Diverse governing equations in physical systems

Cahn-Hilliard and Allen-Cahn equations^{46,47}. Phase-field models represent a powerful computational framework for simulating microstructural evolution in materials undergoing phase transformations. By employing a diffuse-interface description of phase boundaries, these models elegantly circumvent the computational complexity of explicit interface tracking. Their versatility has enabled widespread applications across physics, chemistry, and biology, particularly in studying phenomena such as solidification, grain growth, and pattern formation.

The Allen-Cahn (AC) and Cahn-Hilliard (CH) equations serve as fundamental PDEs within this framework. The CH equation governs the evolution of a conserved concentration field driven by chemical potential gradients:

$$\frac{\partial c}{\partial t} = \nabla \cdot (D(c)c\nabla\mu) \quad (17)$$

where $c(\mathbf{x}, t)$ is the conserved concentration field, $D(c)$ is the concentration-dependent diffusivity, and $\mu = \delta F/\delta c$ is the chemical potential derived from the variational derivative of the free energy

functional F .

For non-conserved order parameters, the AC equation incorporates a state-dependent kinetic coefficient $R_0(c)$:

$$\frac{\partial c}{\partial t} = -R_0(c)\mu \quad (18)$$

This formulation provides a linearized representation of Allen-Cahn reaction kinetics, capturing the nonlinear dependence of reaction rates on thermodynamic driving forces.

The chemical potential μ , central to both equations, takes the form:

$$\mu = \mu_{\text{hom}}(c) - \kappa \nabla^2 c \quad (19)$$

where $\mu_{\text{hom}}(c)$ is the homogeneous (bulk) part of the chemical potential, κ is a positive gradient energy constant, and $-\kappa \nabla^2 c$ represents the gradient energy term, introducing interfacial effects that result in diffuse interfaces between different phases.

In this work, we use the regular solution model, or equivalently Flory-Huggins model, which has been widely used to model the free energy of phase separating systems, ranging from materials science to biology^{13,58}. With this model, the homogeneous free energy per molecule (or per crystal lattice site) normalized by thermal energy is $g_{\text{hom}}(c) = c \log c + (1 - c) \log(1 - c) + \chi c(1 - c)$. Hence the normalized homogeneous part of the chemical potential is $\mu_{\text{hom}}(c) = \frac{dg_{\text{hom}}}{dc} = \log c(1 - c)^{-1} + \chi(1 - 2c)$ where we set $\chi = 3$. The normalized kinetic coefficient is $R_0(c) = c(1 - c)$ where the kinetic constants are omitted since it can be used to normalized time. Similarly, the normalized diffusivity is $D(c) = 1 - c$ to account for the reduction of free space for diffusion when the lattice becomes occupied^{13,59}. Since scaling the length scales according, we can set the gradient energy coefficient κ is set to 1.

Deterministic Kardar-Parisi-Zhang (dKPZ) equation⁵⁰. The deterministic Kardar–Parisi–Zhang (dKPZ) equation is a widely studied nonlinear partial differential equation that models the evolution of growing interfaces under constant growth rates in the normal direction and with local surface relaxation. It serves as a paradigmatic framework for investigating kinetic roughening phenomena, where fluctuations in interface morphology emerge from the competition between diffusion and nonlinear steepening. The determinant version of the governing equation is given by:

$$\frac{\partial h}{\partial t} = v \nabla^2 h + \frac{\lambda}{2} (\nabla h)^2 \quad (20)$$

where $h(x, t)$ represents the height of the interface over space and time. The term $\nu \nabla^2 h$ accounts for smoothing due to surface tension–driven diffusion, with the diffusion coefficient set to $\nu = 0.1$. The nonlinear term $(\lambda / 2)(\nabla h)^2$ describes the projection of the surface growth in the normal direction onto the vertical direction with $\lambda = -0.5$ controlling the strength and direction of the nonlinear coupling. Together, these terms give rise to the steepening of surface profiles.

Complex Ginzburg-Landau (CGL) equation²². The complex Ginzburg–Landau (CGL) equation is a fundamental model in the study of nonlinear wave dynamics, pattern formation, and spatiotemporal chaos in nonequilibrium systems. It governs the evolution of a complex-valued order parameter under the influence of dispersion, diffusion, and nonlinear self-interaction. This equation captures a rich array of dynamical behaviors, including phase turbulence, defect chaos, and rotating spiral waves observed in chemical reactions, fluid instabilities, and excitable media. The CGL equation is written as:

$$\frac{\partial u}{\partial t} = (1 + i\alpha)\nabla^2 u + u - (1 + i\beta)|u|^2 u \quad (21)$$

where $u(x, t)$ is a complex scalar field representing the amplitude and phase of local oscillations. The term $(1 + i\alpha)\nabla^2 u$ couples spatial diffusion and dispersion, where α controls the strength of linear dispersion. The nonlinear term $(1 + i\beta)|u|^2 u$ introduces amplitude saturation and phase-dependent frequency shifts, where β determines the nonlinearity-induced temporal modulation. In the examples that we studied, we set $\alpha = -0.5$ and $\beta = 1.07$. The balance of these terms leads to spontaneous symmetry breaking, the formation of coherent structures, and sustained spatiotemporal complexity. The CGL framework underlies many universal features of dissipative structures, making it an essential testbed for evaluating data-driven modeling approaches in high-dimensional, pattern-forming, and chaotic systems.

Acknowledgements

This work was supported by the National Key Research and Development Program of China (2025YFE0207400), the National Natural Science Foundation of China (62273197), the Tsinghua-Toyota Joint Research Fund, the Beijing Natural Science Foundation (L233027), and the 111 International Collaboration Project (B25027).

Author Contributions

X.W., H.Z. and B.J. conceived the research. X.W. and X.S. performed the modeling and numerical experiments. X.W., X.S., Q.J., H.S., H.Z, and B.J. interpreted the results. All authors edited and reviewed the manuscript. B.J., H.Z. and H.S. supervised the work.

Competing Interests Statement

The authors declare that they have no conflict of interest.

References

1. Brunton, S. L. & Kutz, J. N. Promising directions of machine learning for partial differential equations. *Nat. Comput. Sci.* 4, 483–494 (2024).
2. Pestourie, R. et al. Physics-enhanced deep surrogates for partial differential equations. *Nat. Mach. Intell.* 5, 1458–1465 (2023).
3. Meigel, F. J. et al. Dispersive transport dynamics in porous media emerge from local correlations. *Nat. Commun.* 13, 5885 (2022).
4. Otsuji, M. et al. A mass conserved reaction-diffusion system captures properties of cell polarity. *PLoS Comput. Biol.* 3, e108 (2007).
5. Zhao, H. et al. Learning heterogeneous reaction kinetics from X-ray videos pixel by pixel. *Nature* 621, 289–294 (2023).
6. Halatek, J. & Frey, E. Rethinking pattern formation in reaction–diffusion systems. *Nat. Phys.* 14, 507–514 (2018).
7. Burkart, T. et al. Control of protein-based pattern formation via guiding cues. *Nat. Rev. Phys.* 4, 511–527 (2022).
8. Virieux, J. P-SV wave propagation in heterogeneous media: velocity-stress finite-difference method. *Geophysics* 51, 889–901 (1986).
9. Chan, T. & Vese, A. Active contours without edges. *IEEE Trans. Image Process.* 10, 266–277 (2001).
10. Short, M. B., Brantingham, P. J., Bertozzi, A. L. & Tita, G. E. Dissipation and displacement of hotspots in reaction-diffusion models of crime. *Proc. Natl Acad. Sci.* 107, 3961–3965 (2010).
11. Smith, G. D. *Numerical Solution of Partial Differential Equations: Finite Difference Methods* (Oxford Univ. Press, 1985).

12. Felippa, C. A. Introduction to finite element methods. *Univ. of Colorado*, 885 (2004).
13. Bazant, M. Z. Theory of chemical kinetics and charge transfer based on nonequilibrium thermodynamics. *Acc. Chem. Res.* 46, 1144–1160 (2013).
14. Pope, S. B. *Turbulent flows* (Cambridge Univ. Press, 2000).
15. Davidson, P. A. *Turbulence: An Introduction for Scientists and Engineers* (Oxford Univ. Press, 2015).
16. Groot, S. R. D. & Mazur, P. *Non-Equilibrium Thermodynamics* (Courier Corporation, 2013).
17. Prigogine, I. *Non-equilibrium statistical mechanics* (Courier Dover Publications, 2017).
18. Cross, M. C. & Hohenberg, P. C. Pattern formation outside of equilibrium. *Rev. Mod. Phys.* 65, 851–1112 (1993).
19. Goldenfeld, N. *Lectures on phase transitions and the renormalization group* (CRC Press, 2018).
20. Cahn, J. W. & Hilliard, J. E. Free energy of a nonuniform system. I. Interfacial free energy. *J. Chem. Phys.* 28, 258–267 (1958).
21. Cahn, J. W. Phase separation by spinodal decomposition in isotropic systems. *J. Chem. Phys.* 42, 93–99 (1965).
22. Aranson, I. S. & Kramer, L. The world of the complex Ginzburg–Landau equation. *Rev. Mod. Phys.* 74, 99–143 (2002).
23. Schmid, P. J. Dynamic mode decomposition of numerical and experimental data. *J. Fluid Mech.* 656, 5–28 (2010).
24. Kutz, J. N., Brunton, S. L., Brunton, B. W. & Proctor, J. L. *Dynamic Mode Decomposition: Data-Driven Modeling of Complex Systems* (SIAM, 2016).
25. Schmid, P. J. Dynamic mode decomposition and its variants. *Annu. Rev. Fluid Mech.* 54, 225–254 (2022).
26. Han, J., Jentzen, A. & Weinan, E. Solving high-dimensional partial differential equations using

- deep learning. *Proc. Natl Acad. Sci.* 115, 8505–8510 (2018).
27. Long, Z., Lu, Y., Ma, X. & Dong, B. PDE-Net: learning PDEs from data. In *International Conference on Machine Learning* 3208–3216 (2018).
28. Vinuesa, R. & Brunton, S. L. Enhancing computational fluid dynamics with machine learning. *Nat. Comput. Sci.* 2, 358–366 (2022).
29. Mianroodi, J. R., Siboni, N. H. & Raabe, D. Teaching solid mechanics to Artificial Intelligence—a fast solver for heterogeneous materials. *Npj Comput. Mater.* 7, 99 (2021).
30. Brunton, S. L., Proctor, J. L. & Kutz, J. N. Discovering governing equations from data by sparse identification of nonlinear dynamical systems. *Proc. Natl Acad. Sci.* 113, 3932–3937 (2016).
31. Raissi, M., Perdikaris, P. & Karniadakis, G. E. Physics-informed neural networks: a deep learning framework for solving forward and inverse problems involving nonlinear partial differential equations. *J. Comput. Phys.* 378, 686–707 (2019).
32. Karniadakis, G. E. et al. Physics-informed machine learning. *Nat. Rev. Phys.* 3, 422–440 (2021).
33. Cuomo, S. et al. Scientific machine learning through physics-informed neural networks: where we are and what’s next. *J. Sci. Comput.* 92, 88 (2022).
34. Cai, S., Mao, Z., Wang, Z., Yin, M. & Karniadakis, G. E. Physics-informed neural networks (PINNs) for fluid mechanics: a review. *Acta Mech. Sin.* 37, 1727–1738 (2021).
35. Zhou, J., Li, R. & Luo, T. Physics-informed neural networks for solving time-dependent mode-resolved phonon Boltzmann transport equation. *npj Comput. Mater.* 9, 212 (2023).
36. Wang, F. et al. Physics-informed neural network for lithium-ion battery degradation stable modeling and prognosis. *Nat. Commun.* 15, 4332 (2024).
37. Ren, P., Rao, C., Liu, Y., Wang, J. X. & Sun, H. PhyCRNet: Physics-informed convolutional-recurrent network for solving spatiotemporal PDEs. *Comput. Methods Appl. Mech. Eng.* 389, 114399 (2022).

38. Rao, C. et al. Encoding physics to learn reaction-diffusion processes. *Nat. Mach. Intell.* 5, 765-779 (2023).
39. Lu, L., Jin, P., Pang, G., Zhang, Z. & Karniadakis, G. E. Learning nonlinear operators via DeepONet based on the universal approximation theorem of operators. *Nat. Mach. Intell.* 3, 218–229 (2021).
40. Li, Z. et al. Fourier neural operator for parametric partial differential equations. In *International Conference on Learning Representations*, 1–16 (2021).
41. Guibas, J. et al. Adaptive Fourier neural operators: efficient token mixers for transformers. In *International Conference on Learning Representations*, 1–15 (2022).
42. Xiong, W. et al. Koopman neural operator as a mesh-free solver of non-linear partial differential equations. *J. Comput. Phys.* 113194 (2024).
43. Cao, Q., Goswami, S. & Karniadakis, G. E. Laplace neural operator for solving differential equations. *Nat. Mach. Intell.* 6, 631–640, (2024).
44. Goswami, S., Bora, A., Yu, Y. & Karniadakis, G. E. Physics-informed deep neural operator networks. In *Machine Learning in Modeling and Simulation: Methods and Applications*, 219–254 (Springer International Publishing, Cham, 2023).
45. Li, Z. et al. Physics-informed neural operator for learning partial differential equations. *ACM/JMS J. Data Sci.* 1, 1–27 (2024).
46. Chen, L. Q. Phase-field models for microstructure evolution. *Annu. Rev. Mater. Res.* 32, 113–140 (2002).
47. Steinbach, I. Phase-field models in materials science. *Modell. Simul. Mater. Sci. Eng.* 17, 073001 (2009).
48. Takamoto, M. et al. PDEBench: an extensive benchmark for scientific machine learning. *Adv. Neural Inf. Process. Syst.* 35, 1596–1611 (2022).
49. Ahmed, K., Yablinsky, C. A., Schulte, A., Allen, T. & El-Azab, A. Phase field modeling of the

- effect of porosity on grain growth kinetics in polycrystalline ceramics. *Modell. Simul. Mater. Sci. Eng.* 21, 065005 (2013).
50. Kardar, M., Parisi, G. & Zhang, Y.-C. Dynamic scaling of growing interfaces. *Phys. Rev. Lett.* 56, 889–892 (1986).
51. Zhao, H., Storey, B. D., Braatz, R. D. & Bazant, M. Z. Learning the physics of pattern formation from images. *Phys. Rev. Lett.* 124, 060201(2020).
52. Petersen, B. K. et al. Deep symbolic regression: recovering mathematical expressions from data via risk-seeking policy gradients. In *International Conference on Learning Representations*, 1–26 (2020).
53. Cordonnier, J. B., Loukas, A. & Jaggi, M. On the relationship between self-attention and convolutional layers. In *International Conference on Learning Representations*, 1–18 (2020).
54. Hao, Z. et al. Dpot: Auto-regressive denoising operator transformer for large-scale PDE pre-training. In *International Conference on Machine Learning*, 1–20 (2024).
55. Alberti, S., Dern, N., Thesing, L. & Kutyniok, G. Sumformer: universal approximation for efficient transformers. In *Proceedings of 2nd Annual Workshop on Topological, Algebraic and Geometric Learning Workshops*, 72-86 (2023).
56. Genton, M. G. Classes of kernels for machine learning: a statistics perspective. *J. Mach. Learn. Res.* 2, 299–312 (2001).
57. Rudy, S. H., Brunton, S. L., Proctor, J. L., & Kutz, J. N. Data-driven discovery of partial differential equations. *Sci. Adv.* 3, e1602614 (2017).
58. Brangwynne, C., Tompa, P. & Pappu, R. Polymer physics of intracellular phase transitions. *Nat. Phys.* 11, 899–904 (2015).
59. Bazant, M. Z. Thermodynamic stability of driven open systems and control of phase separation by electro-autocatalysis. *Faraday Discuss.* 199, 423–463 (2017).

Supplementary information

Hierarchical Physics-Embedded Learning for Prediction and Discovery in Spatiotemporal Dynamical Systems

Xizhe Wang^{1*}, Xiaobin Song^{1*}, Qingshan Jia¹, Hao Sun^{2†}, Hongbo Zhao^{3†} and Benben Jiang^{1†}

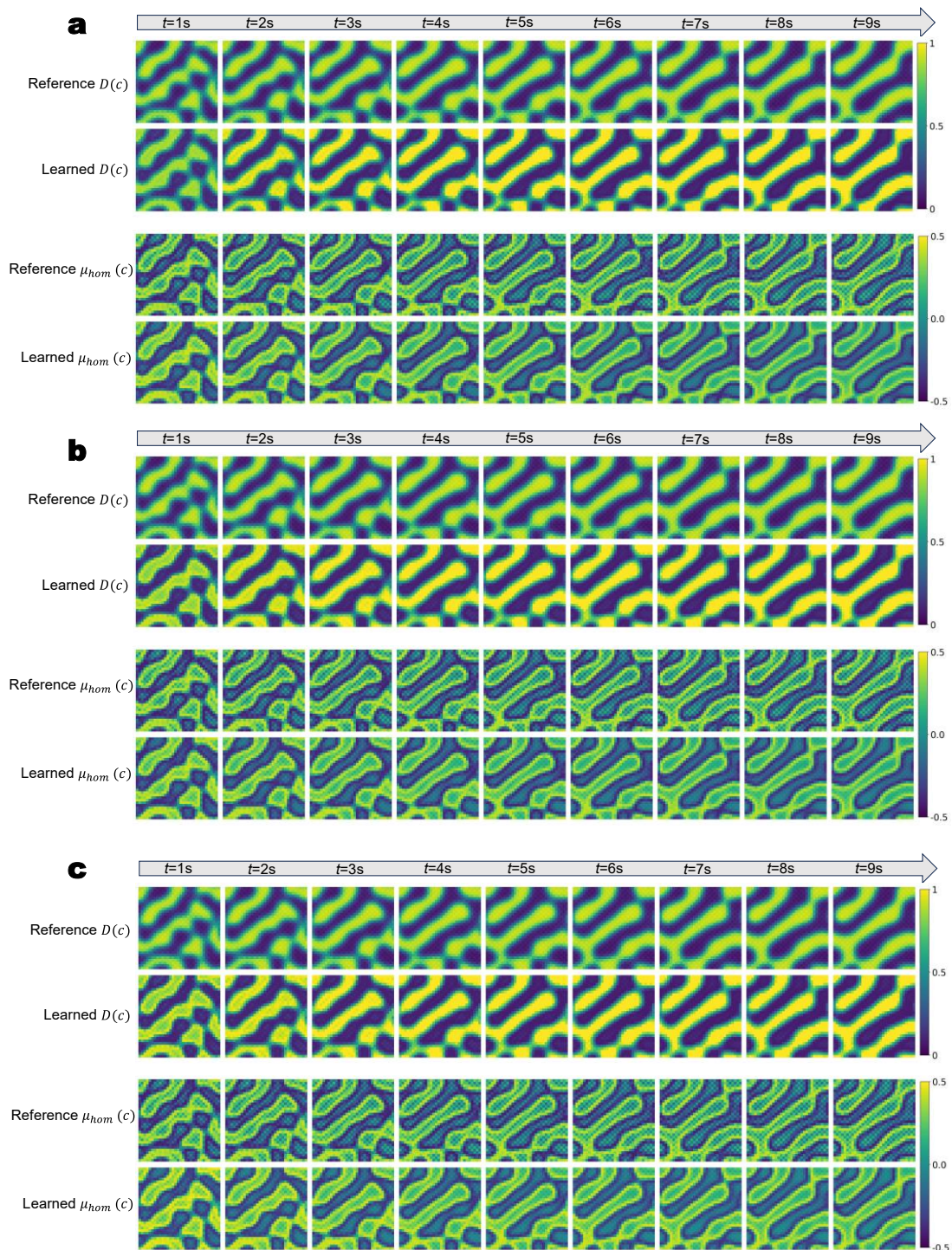
1 CFINS, Department of Automation, Beijing National Research Center for Information Science and Technology, Tsinghua University, Beijing 100084, China

2 Gaoling School of Artificial Intelligence, Renmin University of China, Beijing 100086, China

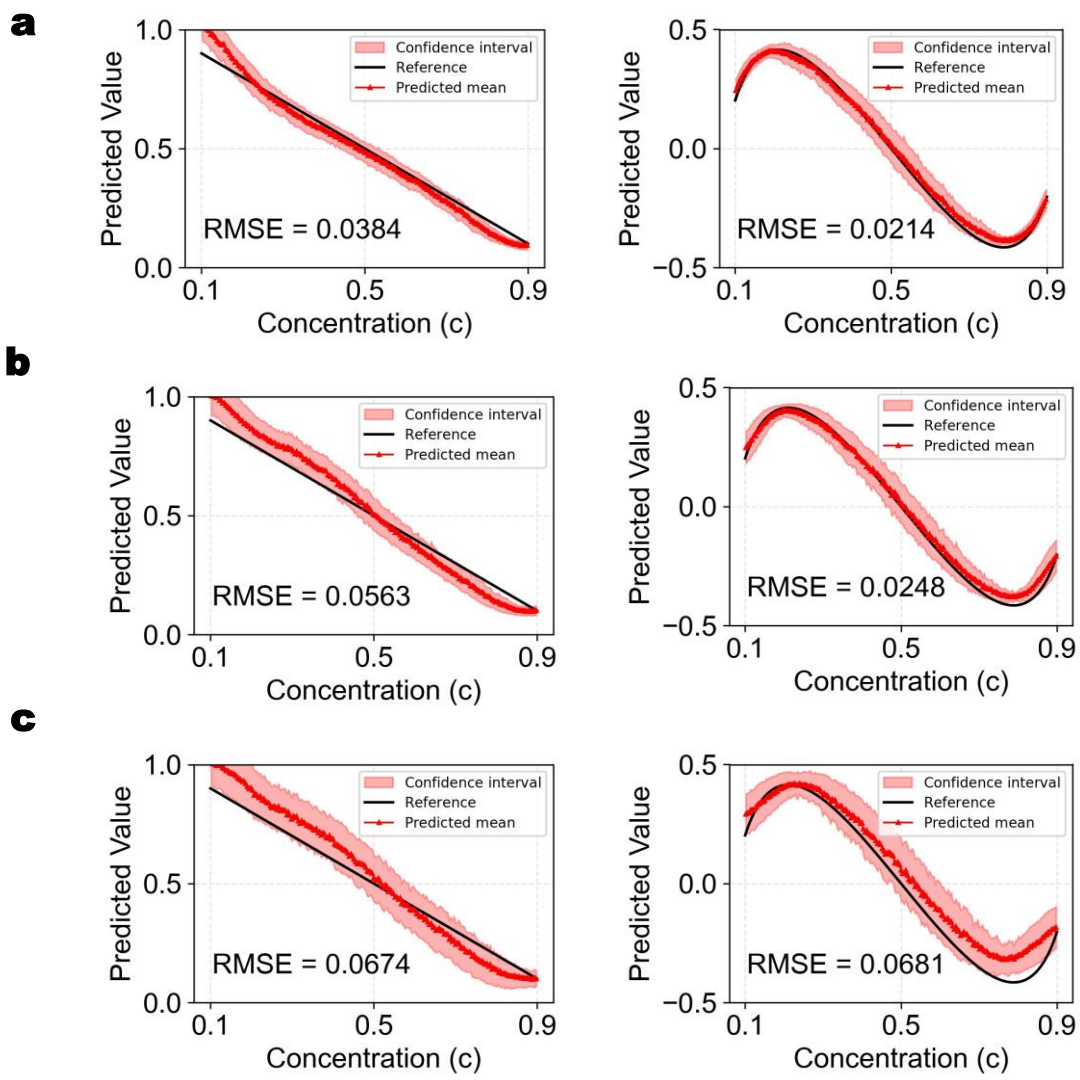
3 Department of Physics, Department of Chemistry and Biochemistry, University of California, San Diego, CA 92093, USA

* These authors contributed equally to this work

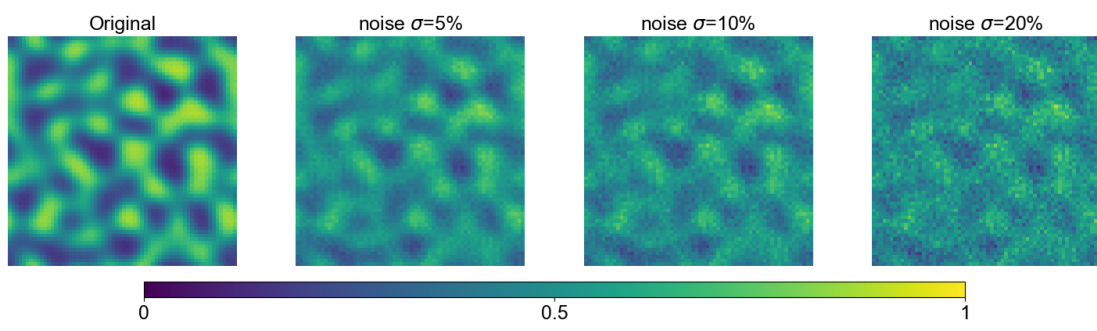
† Corresponding authors



Supplementary Fig. 1 | Predicted evolution of unknown physical terms under varying noise levels. Concentration-dependent diffusivity $D(c)$ and homogeneous chemical potential $\mu_{hom}(c)$ predicted by the HPE-AFNO model under three levels of additive Gaussian noise in the measurement data: (a) 0%, (b) 5%, and (c) 10%. For each case, the top row displays the ground truth, while the bottom row shows the corresponding predictions from the first level of the model, where two separate AFNO channels are respectively assigned to learn $D(c)$ and $\mu_{hom}(c)$. Temporal evolution is shown from left to right, spanning $t = 1s$ to $t = 9s$. The model maintains high predictive accuracy across noise levels, enabling reliable learning of the physical terms and supporting subsequent concentration binning analysis and deep symbolic regression for equation discovery.



Supplementary Fig. 2 | Extraction of functional dependence via concentration binning analysis under varying noise levels. Statistical representations of the concentration-dependent diffusivity $D(c)$ (left panels) and homogeneous chemical potential $\mu_{hom}(c)$ (right panels), derived from the model predictions shown in Supplementary Fig. 1 using concentration binning analysis. Results are presented for three levels of additive Gaussian noise: (a) 0%, (b) 5%, and (c) 10%. For each subplot, model predictions were grouped into discrete concentration intervals and averaged to obtain a smoothed profile of the corresponding physical term, as described in Methods. Black curves represent the ground-truth functions, red curves indicate the predicted means, and shaded bands denote one standard deviation. RMSE values quantify the deviation from the reference expressions. These results demonstrate that the proposed framework consistently extracts accurate functional dependencies across varying noise levels, providing robust inputs for symbolic regression and subsequent closed-form PDE discovery.



Supplementary Fig. 3 | Ground truth data with Gaussian noise contamination at varying levels. The figure illustrates the ground truth data ($\sigma = 0$) and its noisy variants with contamination levels of 5% ($\sigma = 0.05$), 10% ($\sigma = 0.1$), and 20% ($\sigma = 0.2$). The noise intensity increases progressively from left to right.

Supplementary Note 1: Implementation details of HPE-AFNO

We propose Hierarchical Physics-Encoded Adaptive Fourier Neural Operator (HPE-AFNO) to study the nonlinear dynamical system where the spatiotemporal evolution is governed by a partial differential equation (PDE). Let $\mathbf{u}(\mathbf{x}, t)$ denote the state variable (observational data or snapshots collected from experiments or nature), \mathbf{u}_t represent the first-order time derivative of the state variable, and \mathbf{u}_x denote the spatial derivative. Then the PDE can be formulated as:

$$\mathbf{u}_t = \mathcal{F}(\mathbf{u}, \mathbf{u}_x, \mathbf{u}_{xx}, \dots, \mathbf{x}, t)$$

where \mathcal{F} is a nonlinear function involving \mathbf{u} and its spatial derivatives of various orders. To simulate the process of time evolution and reduce the number of parameters, we employ a recurrent network architecture with shared parameters to solve the PDE following the forward Euler scheme:

$$\hat{\mathbf{u}}^{k+1} = \hat{\mathbf{u}}^k + \hat{\mathcal{F}}(\hat{\mathbf{u}}^k, \theta) \delta t$$

where $\hat{\mathbf{u}}^k$ represents the prediction at time t_k , and $\hat{\mathcal{F}}$ is an approximation of \mathcal{F} parameterized by θ . Our HPE-AFNO model is designed for $\hat{\mathcal{F}}$.

For the core architecture of HPE-AFNO, we design a hierarchical architecture that separately approximates low-order spatial features and their combinations to reduce the complexity and improve the accuracy of learning spatial evaluation, as shown in **Fig.1c**, which can be represented as:

$$\hat{\mathcal{F}}(\hat{\mathbf{u}}_k, \theta) = \hat{\mathcal{C}}(\hat{\mathcal{E}}(\hat{\mathbf{u}}^k, \theta_{\mathcal{E}}), \theta_{\mathcal{C}})$$

where $\hat{\mathcal{E}}(\cdot) = (\hat{\mathcal{E}}_1(\cdot), \dots, \hat{\mathcal{E}}_m(\cdot))$ denotes the approximation of m fundamental physical terms parameterized by $\theta_{\mathcal{E}}$, $\hat{\mathcal{C}}(\cdot)$ denotes the approximation of the rule that combines these terms into the time derivative parameterized by $\theta_{\mathcal{C}}$, and $\theta = (\theta_{\mathcal{E}}, \theta_{\mathcal{C}})$.

This hierarchical framework improves the ability to learn higher-order differential operators, aligns with the process of acquiring physical laws, and facilitates the integration of known physical information. For known physical terms, we can directly embed them into our model, which helps speed up training and enhance prediction accuracy. Specifically, known spatial features can be embedded by introducing an additional channel in the first-level AFNO, while known combinations can be integrated by constructing a separate channel that impacts the features extracted by the first-level AFNO, as illustrated in **Fig. 1c**. Notably, we employ first-order difference method to approximate first differentiation considering the speed of training and prediction. For unknown terms or combination relationships, we choose AFNO [1] to extract intricate spatial patterns in the frequency domain, as shown in **Fig. 1a** (we use the [code](https://github.com/NVIDIA/modulus/blob/1f89d93da8cfb0e093bb9ad83f0eadde6c1cd5c9/modulus/models/afno/afno.py) in <https://github.com/NVIDIA/modulus/blob/1f89d93da8cfb0e093bb9ad83f0eadde6c1cd5c9/modulus/models/afno/afno.py>). The relevant parameters for leaning the Allen-Cahn (AC) and Cahn-Hilliard (CH) equations are listed in **Supplementary Table 1**. A Fourier attention layer in AFNO consists of three parts: (1) employ the discrete Fourier transform to mix different tokens: $\mathbf{Z}[i, j, :] = \text{DFT}(\bar{\mathbf{U}})[i, j, :]$ where $\bar{\mathbf{U}} \in \mathbb{R}^{H' \times W' \times d}$ is obtained through patch and position embedding from $\mathbf{U} \in \mathbb{R}^{H \times W}$; (2) multiply the weight matrix $\mathbf{W}_f \in \mathbb{C}^{H' \times W' \times d \times d}$ in the frequency domain to mix different channels: $\bar{\mathbf{Z}}[i, j, :] = \mathbf{W}_f[i, j, :, :] \mathbf{Z}[i, j, :]$; and (3) adopt the inverse discrete Fourier transform: $\mathbf{Y}[i, j] = \text{IDFT}(\bar{\mathbf{Z}})[i, j]$. Furthermore, in the implementation of AFNO, the Fourier attention layer introduces some tricks. For the weight matrix \mathbf{W}_f in step (2), the layer selects a block-diagonal structure that divides $\mathbf{W}_f[i, j, :, :]$ into k weight blocks (i.e. the *number of blocks* in **Supplementary Table 1**) with the size of $(d/k) \times (d/k)$ to reduce

the number of parameters, allow parallel computation, and achieve the effect of multi-head attention mechanism [1]. To further reduce the number of learnable parameters and improve the adaptability, the multilayer perceptron (MLP) with shared parameters is adopted in step (2): $\bar{\mathbf{Z}}[i, j, :] = \mathbf{W}_{f2}\sigma(\mathbf{W}_{f1}\mathbf{Z}[i, j, :]) + \mathbf{b}$ [1]. Moreover, AFNO also employs the soft-thresholding and shrinkage operation: $\bar{\mathbf{Z}}[i, j, :] = \text{Softshrink}_{\lambda}(\mathbf{W}_f[i, j, :, :]\mathbf{Z}[i, j, :])$, where $\text{Softshrink}_{\lambda}(x) = \text{sign}(x) \max\{|x| - \lambda, 0\}$, to sparsify the tokens and increase attention to the important ones [1]. Here λ is a hyperparameter controlling the sparsity and corresponds to the *sparsity threshold* in **Supplementary Table 1**. The meanings of other variables in **Supplementary Table 1** are as follows: *depth* represents the number of Fourier attention layers; *MLP ratio* donates the ratio of the size of latent variable in MLP to the size of input feature; *drop-out rate* represents the drop-out rate in MLP; and *hard thresholding fraction* donates the threshold for constraining the number of modes. When training HPE-AFNO, we utilize the Mean Square Error (MSE) as loss function and employ the Adam optimizer. The training parameters are also listed in **Supplementary Table 1**.

Supplementary Note 2: Baseline methodologies

In this work, we adopt the Physics-encoded Recurrent Convolutional Neural Network (PeRCNN) [2] and the two-dimensional Fourier Neural Operator (FNO-2D) [3] as baseline methods.

Physics-encoded Recurrent Convolutional Neural Network (PeRCNN).

PeRCNN implements a recurrent architecture with shared parameters, implemented through the forward Euler scheme. Unlike HPE-AFNO, PeRCNN introduces a novel convolutional block, referred to as the Π -block, to approximate the non-linear function \mathcal{F} . The Π -block's core innovation lies in its use of the product of convolution. Specifically, Π -block first employs multiple parallel convolutional layers to extract diverse features from the state variable. These features are subsequently fused through element-wise product. Finally, multiple channels are combined through a 1×1 convolutional layer to obtain the desired output. More details can be found in [2].

Two-dimensional Fourier Neural Operator (FNO-2D). FNO-2D is another recurrent model for predicting spatiotemporal PDEs. Unlike HPE-AFNO and PeRCNN, FNO-2D directly leverages state variables from previous time steps to forecast temporal evolution instead of using the forward Euler scheme. Following the PDEBench implementation [4], our FNO-2D model utilizes the predictions from the past three time steps (i.e. $\hat{\mathbf{u}}^{t-2}$, $\hat{\mathbf{u}}^{t-1}$ and $\hat{\mathbf{u}}^t$) to predict $\hat{\mathbf{u}}^{t+1}$: $\hat{\mathbf{u}}^{t+1} = \text{FNO}(\hat{\mathbf{u}}^{t-2}, \hat{\mathbf{u}}^{t-1}, \hat{\mathbf{u}}^t)$. The fundamental idea behind FNO is to operate in the frequency domain. Specifically, FNO first applies a Fourier transform to convert the input variables from the real domain to the frequency domain. Subsequently, multiply a learnable weight matrix in the frequency domain (which corresponds to the convolution operation in the real domain). Finally, the desired output is obtained by performing an inverse Fourier transform to return to the real domain. For more details, please refer to [3].

Supplementary Note 3: Evaluation metrics

To quantitatively assess model performance across both training and testing phases, we adopt the Root Mean Square Error (RMSE) as the primary evaluation metric. RMSE quantifies the average magnitude of error between the predicted and ground truth data, effectively capturing discrepancies in spatial and temporal dynamics.

The RMSE for a single snapshot is calculated as:

$$\text{RMSE} = \sqrt{\frac{1}{N} \sum_{i=1}^N (u_{pred}(i) - u_{true}(i))^2}$$

where N is the total number of spatial grid points (e.g., $64 \times 64 = 4096$), $u_{pred}(i)$ and $u_{true}(i)$ are the predicted and ground truth values, respectively, at grid point i . RMSE is computed for each snapshot and can be averaged over multiple time steps to provide a holistic evaluation of model accuracy. As a metric, RMSE penalizes large errors more heavily than other measures, making it particularly well-suited for high-dimensional systems governed by differential operators. Additionally, its intuitive interpretation as an error magnitude aids in comprehending the model's ability to capture the spatiotemporal dynamics of the system.

Supplementary Note 4: Details of noise implementation

To evaluate the robustness of our framework against noise contamination, Gaussian noise was systematically introduced into the dataset. The noise addition process is defined by the following formula [2]:

$$\text{noise_data} = \text{truth} + R \cdot \sigma \cdot \frac{\max(\text{truth}) - \min(\text{truth})}{2}$$

where $R \sim \mathcal{N}(0,1)$ is a random variable sampled from a standard normal distribution, σ is the noise intensity specified as a fraction of the data range (with values of 0.05 for 5%, 0.1 for 10%, and 0.2 for 20%, see **Supplementary Fig. 3**), and $\max(\text{truth})$ and $\min(\text{truth})$ represent the maximum and minimum values of the ground truth data. This approach ensures that the added noise is proportional to the data range, effectively simulating realistic measurement noise while maintaining precise control over the noise intensity.

Supplementary Note 5: Comparison with existing symbolic regression methods

We compare our hierarchical physics-embedded framework with several representative symbolic regression approaches, including PeRCNN, sparse regression methods such as SINDy [5] and PDE-FIND [6], and end-to-end equation discovery techniques such as deep symbolic regression (DSR) [7] and genetic programming (GP) [8].

PeRCNN combines physics-encoded convolutional architectures with sparse regression to identify governing equations from spatiotemporal data. However, in complex systems with coupled nonlinear dynamics—such as the Cahn–Hilliard equation—PeRCNN often suffers from high reconstruction error. This is primarily because the physical terms must first be approximated through a full-field solution reconstruction, and any inaccuracies in this step inevitably propagate into the subsequent sparse regression, degrading the quality of discovered equations.

Furthermore, the sparse regression stage itself presents inherent challenges. It relies on predefined symbolic libraries and assumes that the target physical terms can be expressed as linear combinations of candidate functions. This not only requires substantial prior knowledge but also limits the model’s capacity to recover non-polynomial or compositional expressions. Its performance deteriorates especially under sparse or noisy measurements, which are typical in real-world scenarios.

End-to-end approaches such as DSR and GP eliminate the reliance on explicit reconstruction steps, instead attempting to directly infer the governing equations from raw data. However, these methods lack the ability to disentangle multiple coupled physical effects. They typically require complete, high-resolution datasets to achieve stable training and meaningful results. Without effective integration of known physical knowledge, their search space remains large, and optimization often results in unstable, inaccurate, or overly complex expressions.

Our framework addresses these limitations through a hierarchical and decoupled discovery process. By first reconstructing spatiotemporal dynamics using physics-embedded learning, we can extract intermediate physical terms that are structurally aligned with the PDE form. These terms are then individually mapped to symbolic expressions using deep symbolic regression guided by reinforcement learning. This two-stage design avoids the error amplification seen in PeRCNN, eliminates the reliance on symbolic libraries, and decouples the discovery of multiple physical terms. Importantly, our method remains effective under sparse and noisy conditions, achieving robust recovery of governing equations even in the absence of dense measurements.

Supplementary Table 1. Hyperparameter list for training HPE-AFNO

Parameters	AFNO model for extracting	AFNO model for combining
	spatial features	spatial features
Model architecture	patch size	[4, 4]
	embedding dimensionality	32
	input channels	1
	output channels	3
	number of blocks	2
	depth	1
	MLP ratio	2.0
	drop-out rate	0.3
	sparsity threshold	0.01
	hard thresholding fraction	1.0
Training	optimizer	Adam
	learning rate	1e-3 (StepLR: step_size=500, gamma=0.5)
	betas	(0.9, 0.999)
	eps	1e-8

Reference

1. Guibas, J. et al. Adaptive Fourier neural operators: efficient token mixers for transformers. Preprint at arXiv:2111.13587 (2021).
2. Rao, C. et al. Encoding physics to learn reaction-diffusion processes. *Nature Mach. Intell.* **5**, 765–779 (2023).
3. Li, Z. et al. Fourier neural operator for parametric partial differential equations. In *International Conference on Learning Representations* (OpenReview.net, 2021).
4. Takamoto, M. et al. PDEBench: an extensive benchmark for scientific machine learning. *Adv. Neural Inf. Process. Syst.* **35**, 1596–1611 (2022).
5. Brunton, S. L., Proctor, J. L. & Kutz, J. N. Discovering governing equations from data by sparse identification of nonlinear dynamical systems. *Proc. Natl Acad. Sci. USA* **113**, 3932–3937 (2016).
6. Rudy, S. H., Brunton, S. L., Proctor, J. L. & Kutz, J. N. Data-driven discovery of partial differential equations. *Sci. Adv.* **3**, e1602614 (2017).
7. Petersen, B. K. et al. Deep symbolic regression: recovering mathematical expressions from data via risk-seeking policy gradients. In *International Conference on Learning Representations* (OpenReview.net, 2020).
8. Augusto, D. A. & Barbosa, H. J. Symbolic regression via genetic programming. In *Proceedings 6th Brazilian Symp. Neural Networks* 173–178 (IEEE, 2000).